

Signatures of first stars in galaxy surveys: Multi-tracer analysis of the supersonic relative velocity effect and the constraints from the BOSS power spectrum measurements

Jaiyul Yoo^{1,2*} and Uroš Seljak^{1,2,3,4}

¹*Institute for Theoretical Physics, University of Zürich, CH-8057 Zürich, Switzerland*

²*Lawrence Berkeley National Laboratory, University of California, Berkeley, CA 94720, USA*

³*Physics Department and Astronomy Department, University of California, Berkeley, CA 94720, USA and*

⁴*Institute for the Early Universe, Ewha Womans University, 120-750 Seoul, South Korea*

We study the effect of the supersonic relative velocity between dark matter and baryons on large-scale galaxy clustering and derive the constraint on the relative velocity bias parameter from the Baryonic Oscillation Spectroscopic Survey (BOSS) power spectrum measurements. Recent work has shown that the relative velocity effect may have a dramatic impact on the star formation at high redshifts, if first stars are formed in minihalos around $z \sim 20$, or if the effect propagates through secondary effects to stars formed at later redshifts. The relative velocity effect has particularly strong signatures in the large scale clustering of these sources, including the BAO position. Assuming that a small fraction of stars in low-redshift massive galaxies retain the memory of the primordial relative velocity effect, galaxy clustering measurements can be used to constrain the signatures of the first stars. Luminous red galaxies contain some of the oldest stars in the Universe and are ideally suited to search for this effect. Using the BOSS power spectrum measurements from the Sloan Data Release 9, in combination with Planck, we derive the upper limit on the fraction of the stars sensitive to relative velocity effect $f_* < 3.3\%$ at the 95% confidence level in the CMASS galaxy sample. If additional galaxy sample not sensitive to the effect is available in a given survey, a joint multi-tracer analysis can be applied to construct a sample-variance cancelling combination, providing a model-independent way to verify the presence of the relative velocity effect in the galaxy power spectrum on large scales. Such a multi-tracer analysis in future galaxy surveys can greatly improve the current constraint, achieving a 0.1% level in f_* .

PACS numbers: 98.80.-k, 98.65.-r, 98.80.Jk, 98.62.Py

I. INTRODUCTION

After the cosmic recombination at $z = 1090$, the cosmic background radiation decouples from the baryon-photon plasma and fades away as the Universe expands and enters the cosmic dark ages [1]. Until the emergence of the first stars, no light but 21cm radiation from neutral hydrogens is emitted in the Universe. Previously, the period of the dark ages to the formation of the first stars was thought to be well described by simple physics that involves the linear evolution of matter and baryons with few chemical reactions and their interaction with photons [2, 3]. However, it was shown in Tseliakhovich and Hirata [4] that a typical velocity difference between baryons and dark matter after the cosmic recombination corresponds to a supersonic flow with Mach number $\mathcal{M} \sim 2$. During the period $z = 15 \sim 100$, most volume in the Universe is filled with supersonic flows and shocks, and the volume with $\mathcal{M} < 1$ is less than 10%. In Dalal et al. [5] it was argued that the effect could dramatically change the fraction of baryons captured in dark matter halos, having no baryons condensing inside halos when the relative velocity is larger than the halo virial velocity, and having baryons inside dark matter halos only in regions where the relative velocity is zero. This and subsequent studies [6–9] showed that these supersonic relative velocities suppress the dark matter halo abundance at low mass, reduce the gas contents in those halos, and boost the minimum cool-

ing mass, which altogether delays and suppresses the formation of the early baryonic structure, by an amount proportional to the local relative velocity.

High-resolution numerical simulations using adaptive-mesh refinement or moving-mesh hydrodynamics techniques [10–12] have confirmed that the relative velocity effect influences the virialization of the gas in minihalos and delays the population III star formation. A series of numerical simulations [9, 13] provide a statistically robust evidence that the gas content is significantly reduced below the characteristic mass scale that is large enough for gas to collapse due to gravity overcoming the pressure gradient. A further numerical study [14] reveals a stunning complexity of gas accretion into the characteristic mass halos and emphasizes consistent treatment of the relative velocity effect in simulations.

Furthermore, the presence of the supersonic relative velocity effect at high redshifts makes the spatial distribution of the star formation highly inhomogeneous, boosting the fluctuation signal by modulating the formation of first stars on very large, hundred (comoving) Megaparsec, scales. This can be detectable in redshifted 21cm observations [5, 15, 16] at $z > 10$ (see also [8, 17]). More importantly, this spatial inhomogeneity is modulated by the relative velocity effect that is coherent on larger scales than the matter density, exhibiting a prominent acoustic oscillation structure in the power spectrum [5]. At high redshifts, the relative velocity contribution to the power spectrum is substantially larger than the matter fluctuation contribution, especially on the baryonic acoustic oscillation (BAO) scales.

However, the relative velocity effect decays with redshift

*jyoo@physik.uzh.ch, jyoo@lbl.gov

once the halos that are collapsing have virial velocities larger than the relative velocity between baryons and dark matter. Even though the direct impact of the relative velocity effect on the low-redshift massive galaxies is expected to be negligible, stars that have been formed at high redshifts are still expected to retain the memory of the spatial modulation caused by the relative velocity effect. There are further indirect ways how the effect can be important for stars that are forming at or after reionization, long after the minihalos ceased to be important [5, 12, 18, 19]. Such scenarios include a patchy reionization partially driven by minihalos with the relative velocity effect or inhomogeneous metal enrichment of the first stars in the intergalactic medium, both of which subsequently affect the formation of massive galaxies at late times.

These possibilities imply the spatial modulation of galaxy clustering due to the remaining relative velocity effect. It is shown [18] that due to its acoustic oscillation structure at the BAO scale, the relative velocity effect, if unaccounted for, can bias the measurements of the BAO peak position, but if accounted for, its signatures are sufficiently different that it does not bias the estimate of the dark energy equation-of-state or inflate the parameter constraints. Furthermore, the presence of the relative velocity effect in galaxy clustering can be unambiguously identified in the galaxy bispectrum on large scales, although those constraints are not as strong as direct power spectrum constraints.

Here we extend the galaxy clustering analysis [18] of the relative velocity effect and investigate the synergy effect of the multi-tracer analysis. The multi-tracer analysis [20] is developed to take advantage of the fact that the same underlying matter distribution is probed by different tracers and the sampling variance stochasticity can be completely removed by constructing a particular combination of different tracers. This technique has been applied to constraining the growth of structure from the redshift-space distortion [21–24] and measuring the relativistic effect and the primordial non-Gaussianity [25–27]. We use the multi-tracer analysis to improve the constraint on the relative velocity effect and provide a model-independent way to verify its presence in the galaxy power spectrum. Moreover, we apply our formalism of the relative velocity effect in galaxy clustering to the recent galaxy power spectrum measurements [28] from the Baryonic Oscillation Spectroscopic Survey (BOSS; [29]) to derive for the first time the constraint on the fraction of the first stars contained in the galaxy sample.

The organization of the paper is as follows. In Sec. II, we briefly summarize the formalism for computing the relative velocity effect and contrast the acoustic oscillation structures in the matter and the relative velocity distributions. In Sec. III, we present a comprehensive study of the relative velocity effect in galaxy clustering. In the presence of the relative velocity effect, the galaxy power spectrum and the cross-power spectrum are computed in Sec. III A and Sec. III B, and a particular combination of two galaxy samples is constructed to eliminate the leading-order sample variance in Sec. III C. A full covariance matrix of the auto- and the cross-power spectra is computed in Sec. III D, and the shift in the BAO peak position is quantified for the auto- and the cross-power spec-

tra in Sec. III E. The relative velocity effect on the auto- and the cross-correlation functions are studied in Sec. III F and Sec. III G.

In Sec. IV, we analyze the BOSS power spectrum measurements and derive for the first time the constraint on the relative velocity effect in the galaxy sample. Looking to the future, we forecast the constraint on the relative velocity effect, providing a guidance to the multi-tracer analysis in future galaxy surveys in Sec. V. Finally, we summarize our results and discuss the implications of our results on relating the current and the future constraint to the primordial galaxy formation history in Sec. VI. For numerical calculations, we adopt a flat Λ CDM universe with the fiducial cosmological parameters consistent with the recent analysis of the *Planck* satellite mission [1]: The scalar spectral index $n_s = 0.968$ and its running $\alpha_s = 0$ of the primordial curvature power spectrum with its normalization $A_s = 2.46 \times 10^{-9}$ at $k_0 = 0.002 \text{ Mpc}^{-1}$, the matter density $\omega_m = \Omega_m h^2 = 0.140$, the baryon density $\omega_b = \Omega_b h^2 = 0.0222$, the dark energy density $\omega_{\text{de}} = \Omega_{\text{de}} h^2 = 0.328$ (the Hubble parameter $h^2 = \omega_m + \omega_{\text{de}} = 0.68^2$).

II. RELATIVE VELOCITY BETWEEN BARYONS AND DARK MATTER

We begin by defining our convention for various transfer functions that are used in our calculations. In linear theory, perturbations at each wave mode grow only in amplitude given the initial conditions, such that its stochastic nature of perturbations can be separated from the deterministic growth. The former is characterized by the curvature perturbation $\varphi(\mathbf{k})$ in the comoving gauge, when the wave mode exits the horizon during the inflationary period. For the Gaussian initial conditions, the primordial curvature is fully characterized by its power spectrum

$$\Delta_\varphi^2(k) = \frac{k^3}{2\pi^2} P_\varphi(k) \equiv A_s \left(\frac{k}{k_0} \right)^{n_s-1}, \quad (1)$$

where the normalization amplitude is $A_s = 2.46 \times 10^{-9}$ at the pivot scale $k_0 = 0.002 \text{ Mpc}^{-1}$ and the spectral index is $n_s = 0.968$, consistent with the recent Planck results [1]. The deterministic growth from the initial conditions is captured by the transfer function $T(k, z)$ for each perturbation variable, e.g.,

$$\delta_m(\mathbf{k}, z) = T_m(k, z) \varphi(\mathbf{k}), \quad (2)$$

for the dark matter density at z (similarly the subscript b is used for baryons). The transfer functions depend solely upon the wave amplitude and redshift. In practice, we use the public Boltzmann code CMBFAST [30] to compute the transfer functions for dark matter $T_m(k, z)$ and baryons $T_b(k, z)$.

The velocities of dark matter and baryons are also computed in a similar manner. Assuming no vorticity $\nabla \times \mathbf{v} = 0$, the velocity vector is fully described by its scalar perturbation

$$\mathbf{v}_m(\mathbf{k}, z) = -\frac{i\mathbf{k}}{k} v_m(\mathbf{k}, z), \quad (3)$$

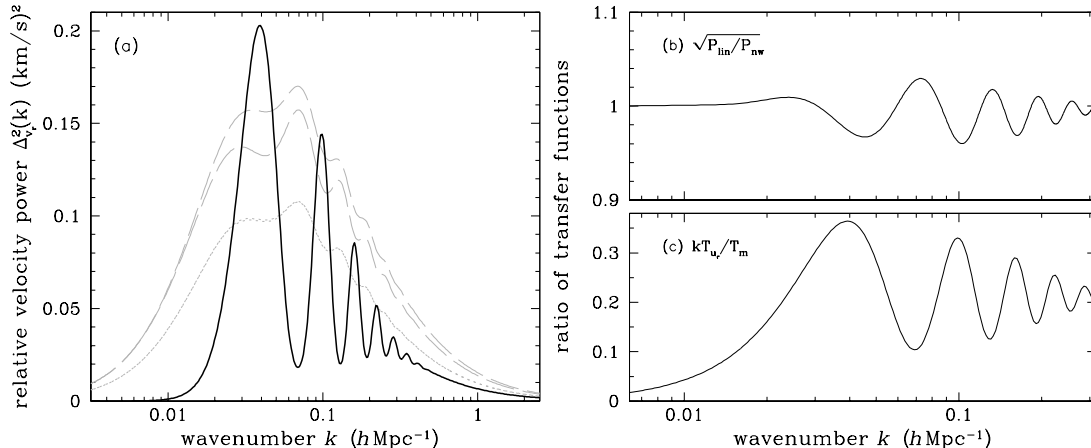


FIG. 1: Relative velocity power spectrum and its transfer functions. *Left*: Solid curve shows the dimensionless relative velocity power spectrum $\Delta_{v_r}^2(k)$ at $z = 15$, and the rms relative velocity is $\sigma_{v_r} \simeq 0.3 \text{ km s}^{-1}$. Velocity power spectra $\Delta_v^2(k)$ and its scaled power spectra $\Delta_v^2(k)/k^2$ for baryon (upper) and dark matter (lower) are shown as gray dotted and dashed curves, respectively (two gray dotted curves largely overlap with each other). Their amplitude is arbitrarily reduced in comparison to $\Delta_{v_r}^2(k)$. While the relative velocity (solid) is sourced by velocities (dotted), its oscillation is *not* in phase with baryon and dark matter velocities. *Right*: Acoustic oscillation structure at $z = 0.57$ in the matter transfer function (b) and in the relative velocity transfer function (c). The oscillation amplitude ($\sim 100\%$) is significantly larger in the relative velocity transfer function than in the matter transfer function ($\sim 5\%$).

and the scalar part is again computed by using the transfer function from CMBFAST

$$v_m(\mathbf{k}, z) = T_{v_m}(k, z) \varphi(\mathbf{k}), \quad (4)$$

which defines the velocity transfer function for dark matter. The conservation equation yields that the velocity transfer function is related to the matter transfer function as

$$\frac{d}{d\tau} T_m(k, z) = -k T_{v_m}(k, z), \quad (5)$$

where τ is the conformal time. The relative velocity of baryons and dark matter is defined as $\mathbf{v}_r = \mathbf{v}_b - \mathbf{v}_m$, and so is the transfer function $T_{v_r} = T_{v_b} - T_{v_m}$. We often use the dimensionless relative velocity

$$u_r(\mathbf{k}, z) \equiv \frac{v_r(\mathbf{k}, z)}{\sigma_{v_r}} = \frac{T_{v_r}(k, z)}{\sigma_{v_r}} \varphi(\mathbf{k}) \equiv T_{u_r}(k, z) \varphi(\mathbf{k}), \quad (6)$$

normalized by the one-dimensional root-mean-square of the relative velocity

$$\sigma_{v_r}^2(z) = \frac{1}{3} \langle \mathbf{v}_r \cdot \mathbf{v}_r \rangle = \frac{1}{3} \int d \ln k T_{v_r}^2(k, z) \Delta_\varphi^2(k). \quad (7)$$

At the recombination, the relative velocity between dark matter and baryons is $\sim 30 \text{ km s}^{-1}$, and it strictly falls off as $1 + z$ as the universe expands, since they both respond to gravity in the same way. Figure 1a shows the relative velocity power spectrum at $z = 15$. We see that it retains prominent oscillation structure. Gray dotted curves show the velocity power spectra for dark matter and baryons (almost identical) at the same redshift but with the amplitude arbitrarily

reduced by 10^5 to compare its oscillation structure with the relative velocity power spectrum (solid). For further comparison, gray dashed curves show the scaled matter power spectrum $\Delta_m^2(k)/k^2$ (lower) and the scaled baryon power spectrum $\Delta_b^2(k)/k^2$ (upper). The difference of their time derivatives is proportional to the relative velocity power spectrum $\Delta_{v_r}^2(k)$ (solid). The oscillation phase of the relative velocity power spectrum is different from the the velocities of dark matter and baryons, despite their common origin.

Figure 1b and 1c further compare the oscillation structure in the matter transfer function and the relative velocity transfer function at $z = 0.57$. In Fig. 1b, the linear matter power spectrum is divided by the no-wiggle power spectrum [31] to highlight the oscillation structure without the broad-band shape of the matter power spectrum.¹ The oscillation amplitude is rather small $\sim 5\%$ in the matter transfer function, while the oscillation amplitude is fractionally order one in the relative velocity transfer function in Fig. 1c. The acoustic oscillation in the relative velocity power spectrum is *not* in phase with the matter power spectrum. Of course this ratio shows the maximal effect at $z = 0.57$ and in reality the effect will be much smaller since only a small fraction of stars is modulated by the relative velocity effect.

¹ The ratio of the matter power spectrum to the no-wiggle power spectrum is plotted in Fig. 1b of Yoo et al. [18]. The x -axis in their Fig. 1b is in units of Mpc^{-1} , instead of $h\text{Mpc}^{-1}$, while its bottom panel has the x -axis in units of $h\text{Mpc}^{-1}$, as is indicated.

III. RELATIVE VELOCITY EFFECT IN GALAXY CLUSTERING

The relative velocity between dark matter and baryons allows separation between baryons and dark matter within halos. Especially at high redshift, when the dark matter halos have shallow gravitational potential, the relative velocity can be supersonic, advecting baryons out of dark matter halos and preventing the formation of baryonic structure [4, 6]. A series of numerical simulations have verified the relative velocity effect on the early structure formation [8–14]. The suppression or the formation of the early baryonic structure is therefore spatially modulated by the relative velocity effect, and its correlation length is set by the acoustic oscillation of the relative velocity [5].

The presence of the relative velocity effect can affect the spatial clustering of the low-redshift massive galaxies, where galaxy clustering measurements are performed. However, it is more difficult in this case to compute the amplitude of the relative velocity effect or to predict the existence of the relic memory of the primordial relative velocity effect. Here we present various ways to identify the relative velocity effect in galaxy clustering measurements and discuss the impact of the relative velocity effect on the BAO measurements, if the relative velocity effect persists.

A. Power Spectrum

Following the procedure in Yoo et al. [18], a galaxy population at low redshift is modeled with two nonlinear galaxy bias parameters b_1 and b_2 and the relative velocity bias parameter b_r as

$$\delta_g(\mathbf{x}) = b_1 \delta_m(\mathbf{x}) + \frac{b_2}{2} [\delta_m^2(\mathbf{x}) - \sigma_m^2] + b_r [u_r^2(\mathbf{x}) - \sigma_{u_r}^2], \quad (8)$$

where the relative velocity $u_r = |\mathbf{u}_r|$ is computed at the linear order and the matter density is computed to the second order in perturbations. The relative velocity bias parameter characterizes our ignorance of the relic amplitude of the remaining relative velocity effect in low-redshift galaxy populations, and the nonlinear galaxy bias parameters are the lowest order coefficients of the local matter density expansion that relate to the galaxy number density (the third-order galaxy bias parameters b_3 and subsequent terms are ignored).

The auto-power spectrum of the galaxy sample described in Eq. (8) can be computed [18] to the second order in power spectrum as

$$P_g(\mathbf{k}) = b_1^2 P_{\text{NL}}(\mathbf{k}) + \int \frac{d^3\mathbf{q}}{(2\pi)^3} P_m(q) P_m(|\mathbf{k} - \mathbf{q}|) \left[\frac{1}{2} b_2^2 + 2 b_1 b_2 F_2(\mathbf{q}, \mathbf{k} - \mathbf{q}) + 4 b_1 b_r F_2(\mathbf{q}, \mathbf{k} - \mathbf{q}) G_u(\mathbf{q}, \mathbf{k} - \mathbf{q}) + 2 b_2 b_r G_u(\mathbf{q}, \mathbf{k} - \mathbf{q}) + 2 b_r^2 G_u(\mathbf{q}, \mathbf{k} - \mathbf{q})^2 \right], \quad (9)$$

where $P_{\text{NL}}(\mathbf{k})$ and $P_m(\mathbf{k})$ are the nonlinear and the matter power spectrum and the relative velocity kernel and the nonlinear matter evolution kernel are

$$G_u(\mathbf{k}_a, \mathbf{k}_b) = -\frac{T_{u_r}(k_a)}{T_m(k_a)} \frac{T_{u_r}(k_b)}{T_m(k_b)} \frac{\mathbf{k}_a \cdot \mathbf{k}_b}{k_a k_b}, \quad (10)$$

$$F_2(\mathbf{k}_a, \mathbf{k}_b) = \frac{5}{7} + \frac{2}{7} \left(\frac{\mathbf{k}_a \cdot \mathbf{k}_b}{k_a k_b} \right)^2 + \frac{\mathbf{k}_a \cdot \mathbf{k}_b}{2} \left(\frac{1}{k_a^2} + \frac{1}{k_b^2} \right).$$

We use the HALOFIT [32] to compute the nonlinear matter power spectrum. The derivation and the computation of the power spectrum in Eq. (9) can be found in Appendix A of Yoo et al. [18]. Apparent from the proportionality of the galaxy bias parameters, each term in Eq. (9) represents the auto- and the cross-contributions of the nonlinear matter evolution ($\sim b_1$), nonlinear galaxy bias ($\sim b_2$), and the relative velocity effect ($\sim b_r$).

Figure 2a illustrates the galaxy power spectrum and the contributions of its individual components in Eq. (9). As our fiducial model, we assume that the galaxy sample has bias parameters $(b_1, b_2) = (2, 1)$ and the relative velocity bias parameter $b_r = 0.04$. The horizontal gray line indicates the

approximate level of the shot-noise contribution $\sqrt{2}/\bar{n}_g$ to the galaxy power spectrum, where we assume the galaxy number density is $3 \times 10^{-4} (h^{-1} \text{Mpc})^{-3}$. The factor $\sqrt{2}$ arises, as we plot the power spectrum variance in the absence of sample variance (see Sec. III D for details). The major contribution to the galaxy power spectrum $P_g(k)$ (thick solid) is the nonlinear matter power spectrum (thick dotted) on all scales shown in Figure 2. However, the individual components shown as different curves contribute to the galaxy power spectrum at various level at different scales, given the fiducial values of the bias parameters. Dashed and dotted curves show the contributions of the nonlinear galaxy bias that are proportional to b_2^2 and $b_1 b_2$, respectively. While their contributions can be as large as 10% of the total power spectrum at $k \sim 0.3 h \text{Mpc}^{-1}$, they are largely featureless and smooth, which can be readily modeled as a smooth broad-band power.

The relative velocity effects are illustrated as solid, dot-dashed and long dashed curves that are respectively proportional to b_r^2 , $b_2 b_r$, and $b_1 b_r$. The relative velocity power spectrum (solid) is significant on large scales, amounting to more than 10% at $k < 0.01 h \text{Mpc}^{-1}$, but it declines as k^{-4} on smaller scales, where the BAO peak position is best measured.

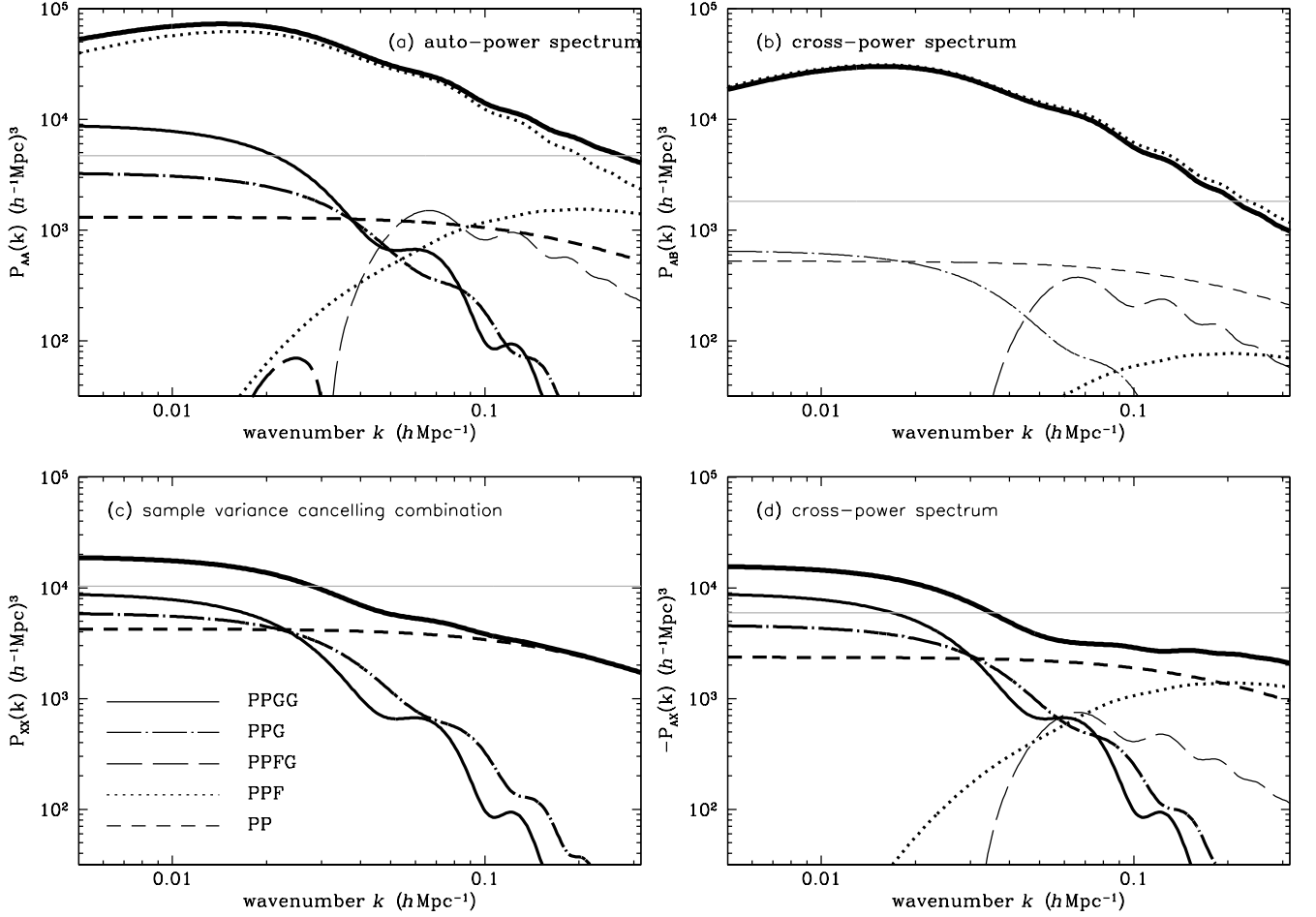


FIG. 2: Auto and cross power spectra of two galaxy samples. The galaxy sample A is assumed to have bias parameters ($b_1 = 2$, $b_2 = 1$, $b_r = 0.04$) and the galaxy sample B has bias parameters ($b_1 = 1$, $b_2 = -0.4$), but without the relative velocity effect ($b_r = 0$). Top panels show the auto (left) and the cross (right) power spectra (thick solid) and their individual contributions (various curves). Dotted curves that closely follow the thick curves show the nonlinear matter power spectrum. Two galaxy samples can be properly combined as in Eq. (13) to construct another tracer X , cancelling the sample variance in Eq. (15). Bottom panels show the auto (left) power spectrum of the tracer X and its cross (right) power spectra with the galaxy sample A . Individual contributions to the total power spectra are shown in all panels as solid, representing the contribution that involves the integral of $b_r^2 P_m(\mathbf{q}) P_m(|\mathbf{k} - \mathbf{q}|) G_u^2(\mathbf{q}, \mathbf{k} - \mathbf{q})$, dot-dashed for $b_r P_m P_m G_u$, long dashed for $b_r P_m P_m F_2 G_u$, dotted for $P_m P_m F_2$, and short dashed for $P_m P_m$. These components are positive (negative) when shown as thick (thin) curves, and they are abbreviated in Panel (c) as PPGG, PPG, PPF, and PP. Also note that each component is proportional to a different combination of the galaxy bias parameters indicated in Eqs. (9), (12), (16), (18), in addition to the relative velocity bias parameter b_r . The horizontal gray lines show the diagonal element of the covariance matrix in the absence of sample variance, approximately equivalent to the shot-noise contribution (see Sec. III D). It is assumed that the number densities of the tracers are $\bar{n}_g = 3 \times 10^{-4} (h^{-1} \text{Mpc})^{-3}$ and $\bar{n}_g = 10^{-3} (h^{-1} \text{Mpc})^{-3}$, respectively.

This effect is still an important factor at the percent level, determining the shift in the BAO peak position (see Sec. III E). However, for the relative velocity bias larger than the fiducial value $b_r/b_1 = 0.02$, the auto contribution of the relative velocity effect dominates over the other contributions on all scales. Similarly, the dot-dashed curve represents the coupling of the relative velocity effect and the nonlinear galaxy bias, in proportion to $b_2 b_r$, and in a similar shape. The oscillation structure of the both contributions arises due to the relative velocity kernel G_u , and its convolution with the matter power spectrum

on large scales becomes constant as $G_u(\mathbf{k}, \mathbf{k}) \propto k^{-2}$. Last, the long dashed curve represents the contribution of the relative velocity effect and the nonlinear matter evolution, constituting the dominant contribution of the relative velocity effect at the BAO scale. Due to the nonlinear matter kernel F_2 , this contribution declines rather slowly with wavenumber, while it retains the oscillation structure.

All of the relative velocity effects and the nonlinear effects are at the percent level or smaller on most scales, given that the total galaxy power spectrum (thick solid) is largely deter-

mined by the matter power spectrum (thick dotted). However, with high precision measurement of the BAO peak position, small but non-negligible contributions with oscillation structure can shift the BAO peak position. In Sec. III E, we quantify the BAO peak shift in the galaxy power spectrum due to the relative velocity effect.

B. Cross Power Spectrum

In the past few decades, there have been rapid developments in large-scale galaxy surveys, and the sheer number has dramatically increased (e.g., see [33]). In this golden age of large-scale surveys, it is quite common and desirable that two separate and independent surveys are designed to cover, albeit partially, the same sky area, generating the synergy effect and providing ways to check systematic errors.

Here we consider another galaxy sample measured in the

survey: Low-mass star-forming galaxies that form at low redshift after generations of old stars evolved away long time ago. The relative velocity effect in those galaxy samples is substantially diluted or nearly absent. To avoid confusion, we use super- or sub-script A and B to refer to each galaxy sample. The galaxy sample A representing massive old and red galaxies with the relative velocity effect is described by Eq. (8). We model the low-mass galaxy sample B with another set of bias parameters

$$\delta_g^B(\mathbf{x}) = b_1^B \delta_m(\mathbf{x}) + \frac{b_2^B}{2} [\delta_m^2(\mathbf{x}) - \sigma_m^2], \quad (11)$$

where the relative velocity bias parameter is set $b_r^B = 0$. The auto-power spectrum of the galaxy sample B can be readily computed by using Eq. (9) with the bias parameters replaced by (b_1^B, b_2^B) . With two galaxy samples in the survey, we can measure their cross-power spectrum,

$$P_{AB}(\mathbf{k}) = b_1^A b_1^B P_{\text{NL}}(\mathbf{k}) + \int \frac{d^3 \mathbf{q}}{(2\pi)^3} P_m(q) P_m(|\mathbf{k} - \mathbf{q}|) \left[\frac{1}{2} b_2^A b_2^B + (b_1^A b_2^B + b_2^A b_1^B) F_2(\mathbf{q}, \mathbf{k} - \mathbf{q}) \right. \\ \left. + 2b_r^A b_1^B F_2(\mathbf{q}, \mathbf{k} - \mathbf{q}) G_u(\mathbf{q}, \mathbf{k} - \mathbf{q}) + b_r^A b_2^B G_u(\mathbf{q}, \mathbf{k} - \mathbf{q}) \right]. \quad (12)$$

Figure 2b depicts the cross-power spectrum $P_{AB}(k)$ of the galaxy sample A in Fig. 2a and the galaxy sample B , where we assume the bias parameters for the galaxy sample B are $(b_1^B, b_2^B) = (1, -0.4)$ and the number density is $10^{-3}(h^{-1}\text{Mpc})^{-3}$. Low-mass star forming galaxies are known to be less biased but more abundant (e.g., see [34]). Since we sample two discrete but distinct objects, there is no shot-noise contribution to the cross-power spectrum $P_{AB}(k)$. However, there exist the shot-noise contributions from each galaxy sample to the power spectrum variance, and the horizontal gray line shows this contribution $\sqrt{1/\bar{n}_g^A \bar{n}_g^B}$ in the absence of sample variance.

Similarly to the auto-power spectrum $P_{AA}(k)$ in Fig. 2a, the dominant contribution to the cross-power spectrum (thick solid) is the matter power spectrum (thick dotted). The contributions of the nonlinear galaxy bias ($b_2^A b_2^B$; dashed) and its coupling with the nonlinear matter evolution ($b_1^A b_2^B + b_2^A b_1^B$; dotted) are also in similar shape, but the former is now negative as $b_2^B < 0$ for low mass galaxies. In regard to the relative velocity contributions to the cross-power spectrum, the notable difference compared to the auto-power spectrum $P_{AA}(k)$ is the absence of the relative velocity auto-power spectrum. While the coupling of the relative velocity effect and the nonlinear galaxy bias $\propto b_r^A b_2^B$ has a negative sign in the cross power spectrum, the contribution of the relative velocity effect and the nonlinear matter evolution $\propto b_r^A b_1^B$ (long dashed) remains the dominant factor with same sign at the BAO scale as in $P_{AA}(k)$.

Compared to the auto-power spectra $P_{AA}(k)$ and $P_{BB}(k)$, the cross-power spectrum $P_{AB}(k)$ in Fig. 2b provides a new way to constrain the relative velocity effect with signal-to-noise ratio as large as their auto power spectra. However, as two galaxy samples probe the same underlying matter distribution in the survey, the auto- and the cross-power spectra are *not* independent, and their covariance matrix needs to be properly taken into consideration (see Sec. III D).

C. Multi-Tracer Analysis

Since different galaxy samples depend on the same underlying matter distribution, their stochastic nature shares the common origin. Based on this observation, the multi-tracer technique is developed [20] to remove the intrinsic stochasticity by taking ratios of multiple tracers. With shot-noise present in practice, the gain in signal-to-noise ratio is much less than in an idealized situation, but a significant gain is still achievable (e.g., see [23, 24, 26, 27]), especially when combined with the shot-noise cancelling technique [35, 36].

Here we construct a particular combination X , out of the two galaxy samples A and B to eliminate the sample variance

$$n_g^X \equiv V_s [b_1^A \bar{n}_g^A n_g^B(\mathbf{x}) - b_1^B \bar{n}_g^B n_g^A(\mathbf{x})] \quad (13) \\ = \bar{n}_g^X (1 + \delta_X) + \varepsilon_X,$$

where ε_X is the shot-noise, \bar{n}_g^A and \bar{n}_g^B are the mean number densities of each galaxy sample and V_s is the survey volume.

As each galaxy sample is composed of its mean and fluctuation, the combination X can also be decomposed as the mean number density

$$\bar{n}_g^X = V_s \bar{n}_g^A \bar{n}_g^B (b_1^A - b_1^B), \quad (14)$$

and its fluctuation around the mean

$$\delta_X(\mathbf{x}) = \frac{b_1^A \delta_g^B - b_1^B \delta_g^A}{b_1^A - b_1^B} \quad (15)$$

$$P_{XX}(\mathbf{k}) = \int \frac{d^3 \mathbf{q}}{(2\pi)^3} P_m(q) P_m(|\mathbf{k} - \mathbf{q}|) \left[\frac{1}{2} \frac{(b_1^A b_2^B - b_2^A b_1^B)^2}{(b_1^A - b_1^B)^2} + \frac{2(b_1^A b_2^B - b_1^B b_2^A) b_r^A b_1^B}{(b_1^A - b_1^B)^2} G_u(\mathbf{q}, \mathbf{k} - \mathbf{q}) + \frac{2(b_r^A b_1^B)^2}{(b_1^A - b_1^B)^2} G_u^2(\mathbf{q}, \mathbf{k} - \mathbf{q}) \right]. \quad (16)$$

The sample-variance cancelling combination has different shot-noise contribution, as it is the combination of two distinct galaxy samples. Assuming the Poisson shot-noise for each sample, the shot-noise contribution to the power spectrum $P_{XX}(k)$ is

$$N_X \equiv \frac{\langle \varepsilon_X \varepsilon_X \rangle}{(\bar{n}_g^X)^2} = \frac{(b_1^A)^2 \bar{n}_g^A + (b_1^B)^2 \bar{n}_g^B}{\bar{n}_g^A \bar{n}_g^B (b_1^A - b_1^B)^2}. \quad (17)$$

Figure 2c illustrates the auto-power spectrum of the sample-variance cancelling combination. Since the leading contribution of the matter power spectrum is eliminated, there exist no contributions of the coupling with the nonlinear matter evolution, and the amplitude of the power spectrum (thick solid) is overall smaller than those shown in the upper panels. The contribution of the nonlinear galaxy bias (dashed) is the dominant

The sample variance is explicitly eliminated in Eq. (15) to the leading order, though much smaller stochasticity, next to the leading order terms, remains. The power spectrum of the sample-variance cancelling combination is then

contribution on all scales, except on large scales where the relative velocity contributions (solid and dot-dashed) become more important. The advantage of using the sample-variance cancelling combination is that the ratio of the relative velocity effect to the total power spectrum is greatly enhanced and the oscillation structure around $k \sim 0.1 h \text{Mpc}^{-1}$ is largely due to the relative velocity effect, as the leading-order matter density contribution is eliminated. However, the gray horizontal lines show the power spectrum variance $\sqrt{2} N_X$ in case $P_{XX} = 0$, and the shot-noise contribution to the power spectrum $P_{XX}(k)$ is non-negligible except on large scales.

With the combination X in addition to two galaxy samples A and B , we can also construct the cross-power spectrum of the sample-variance cancelling combination and the galaxy sample

$$P_{AX}(\mathbf{k}) = \int \frac{d^3 \mathbf{q}}{(2\pi)^3} P_m(q) P_m(|\mathbf{k} - \mathbf{q}|) \left[\frac{1}{2} \frac{b_2^A (b_1^A b_2^B - b_1^B b_2^A)}{b_1^A - b_1^B} + \frac{b_1^A (b_1^A b_2^B - b_1^B b_2^A)}{b_1^A - b_1^B} F_2(\mathbf{q}, \mathbf{k} - \mathbf{q}) \right. \quad (18)$$

$$\left. - \frac{2b_1^A b_1^B b_r^A}{b_1^A - b_1^B} F_2(\mathbf{q}, \mathbf{k} - \mathbf{q}) G_u(\mathbf{q}, \mathbf{k} - \mathbf{q}) + \frac{b_r^A (b_1^A b_2^B - 2b_1^B b_2^A)}{b_1^A - b_1^B} G_u(\mathbf{q}, \mathbf{k} - \mathbf{q}) - \frac{2b_1^B (b_r^A)^2}{b_1^A - b_1^B} G_u^2(\mathbf{q}, \mathbf{k} - \mathbf{q}) \right],$$

and the shot-noise contribution to the cross-power spectrum $P_{AX}(k)$ is

$$N_{AX} \equiv \frac{\langle \varepsilon_A \varepsilon_X \rangle}{\bar{n}_g^A \bar{n}_g^X} = \frac{b_1^B}{\bar{n}_g^A (b_1^B - b_1^A)}. \quad (19)$$

Figure 2d shows the cross-power spectrum $P_{AX}(k)$ of the sample-variance cancelling combination with the galaxy sample A . The cross-power spectrum $P_{AX}(k)$ is similar to the auto-power spectrum $P_{XX}(k)$, as it is constructed from the sample-variance cancelling combination, while it retains some of the cross-contributions from the galaxy sample A . As the combination $n_g^X(\mathbf{x})$ in Eq. (13) is constructed with negative

sign of the galaxy number density $n_g^A(\mathbf{x})$, all the coefficients of the bias parameter combination in Eq. (18) are negative, and we plot $-P_{AX}(\mathbf{k})$. The relative velocity effect is again prominent on large scales, where the signal is somewhat larger than the shot-noise contribution $\sqrt{N_{AX}^2 + N_X/\bar{n}_g^A}$, shown as the gray horizontal line.

D. Covariance Matrix

Out of two galaxy samples in the survey, we can construct three power spectra $P_{AA}(k)$, $P_{BB}(k)$, and $P_{AB}(k)$. Since all

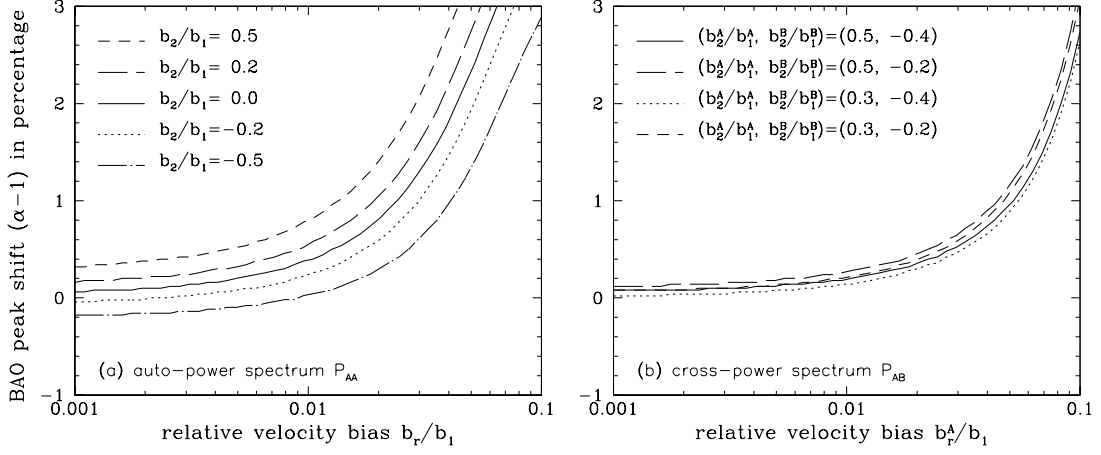


FIG. 3: BAO peak shift in the auto-power spectrum (left) and the cross-power spectrum (right) due to the relative velocity effect. As a function of relative velocity bias parameter b_r/b_1 , the peak shift is obtained by fitting the template power spectrum in Eq. (30) to the full power spectrum, following the procedure in [37]. *Left*: Peak shifts in the auto-power spectrum $P_{AA}(k)$ computed by using Eq. (9) for various values of the nonlinear galaxy bias parameter b_2/b_1 , given the relative velocity effect b_r/b_1 . *Right*: Peak shifts in the cross-power spectrum $P_{AB}(k)$ computed by using Eq. (12) for various combination of the nonlinear bias parameters b_2/b_1 for two different galaxy samples A and B . The relative velocity effect is assumed to be present only in the galaxy sample A , but absent in the galaxy sample B .

of them are tracing the same underlying matter distribution, three power spectra are correlated, and its correlation is described by the covariance matrix. The sample variance cancelling combination in Eq. (15) can be obtained by diagonalizing the covariance matrix of two fluctuations δ_g^A and δ_g^B . To compute the covariance matrix, we first define our estimators for the power spectra of the two galaxy populations:

$$\hat{P}_{AA}(\mathbf{k}) = \frac{1}{V_s} \delta_g^A(\mathbf{k}) \delta_g^{A*}(\mathbf{k}) - \frac{1}{\bar{n}_g^A}, \quad (20)$$

where V_s is the survey volume and \bar{n}_g^A is the number density of the galaxy sample A . Assuming the Poisson shot-noise, the power spectrum estimator in Eq. (20) is unbiased $\langle \hat{P}_{AA}(\mathbf{k}) \rangle = P_{AA}(\mathbf{k})$, and a similar estimator can be defined for the galaxy sample B . In addition, an estimator for the cross power spectrum is

$$\hat{P}_{AB}(\mathbf{k}) = \frac{1}{V_s} \delta_g^A(\mathbf{k}) \delta_g^{B*}(\mathbf{k}), \quad (21)$$

and there is no shot-noise contribution to the cross power spectrum.

Given the power spectrum estimators in Eqs. (20) and (21), the covariance matrix can be readily computed as

$$\text{Cov} \left[\hat{P}_i(\mathbf{k}) \hat{P}_j(\mathbf{k}') \right] = \left\langle \hat{P}_i(\mathbf{k}) \hat{P}_j(\mathbf{k}') \right\rangle - P_i(\mathbf{k}) P_j(\mathbf{k}'), \quad (22)$$

where $i, j = AA, BB, AB$. With many independent Fourier modes added to estimate the power spectra, the power spectrum estimators closely follow a Gaussian distribution, with

which we can analytically derive the covariance matrix. The diagonal components of the covariance matrix are

$$\text{Cov} \left[\hat{P}_{AA} \hat{P}_{AA} \right] = 2 \left(P_{AA} + \frac{1}{\bar{n}_g^A} \right)^2, \quad (23)$$

$$\text{Cov} \left[\hat{P}_{BB} \hat{P}_{BB} \right] = 2 \left(P_{BB} + \frac{1}{\bar{n}_g^B} \right)^2,$$

$$\text{Cov} \left[\hat{P}_{AB} \hat{P}_{AB} \right] = P_{AB}^2 + \left(P_{AA} + \frac{1}{\bar{n}_g^A} \right) \left(P_{BB} + \frac{1}{\bar{n}_g^B} \right),$$

where we suppressed the \mathbf{k} -dependence as each Fourier mode is largely independent and the covariance matrix is nearly diagonal in Fourier space. The off-diagonal components of the covariance matrix are

$$\text{Cov} \left[\hat{P}_{AA} \hat{P}_{BB} \right] = 2 (P_{AB})^2, \quad (24)$$

$$\text{Cov} \left[\hat{P}_{AA} \hat{P}_{AB} \right] = 2 P_{AB} \left(P_{AA} + \frac{1}{\bar{n}_g^A} \right),$$

$$\text{Cov} \left[\hat{P}_{BB} \hat{P}_{AB} \right] = 2 P_{AB} \left(P_{BB} + \frac{1}{\bar{n}_g^B} \right).$$

For the sample-variance cancelling combination X , we have two estimators

$$\hat{P}_{XX}(\mathbf{k}) = \frac{1}{V_s} \delta_X(\mathbf{k}) \delta_X^*(\mathbf{k}) - N_X, \quad (25)$$

$$\hat{P}_{AX}(\mathbf{k}) = \frac{1}{V_s} \delta_g^A(\mathbf{k}) \delta_X^*(\mathbf{k}) - N_{AX}, \quad (26)$$

and their covariance matrix

$$\text{Cov} \left[\hat{P}_{XX} \hat{P}_{XX} \right] = 2 (P_{XX} + N_X)^2, \quad (27)$$

$$\begin{aligned} \text{Cov} \left[\hat{P}_{AX} \hat{P}_{AX} \right] &= (P_{AX} + N_{AX})^2 \\ &+ \left(P_{AA} + \frac{1}{\bar{n}_g^A} \right) (P_{XX} + N_X) . \end{aligned} \quad (28)$$

While the stochastic nature yields irreducible variance of the estimators described by the covariance matrix, their mean can be more accurately estimated by measuring independent Fourier modes available in the survey. The number of Fourier modes in a given survey is often estimated [38] as

$$N_k = \frac{4\pi k^2 \Delta k}{(2\pi)^3} \int_{V_s} d^3\mathbf{x} \left[\frac{\bar{n}_g P_g(\mathbf{k})}{1 + \bar{n}_g P_g(\mathbf{k})} \right]^2 \simeq \frac{4\pi k^2 \Delta k}{(2\pi)^3} V_s , \quad (29)$$

where Δk is the bin width in Fourier modes and we assumed the galaxy samples are sample-variance limited. Since the covariance matrix is computed accounting for the wavevectors \mathbf{k} and $-\mathbf{k}$, the number N_k of wavemodes appears larger by a factor 2 than in the usual calculation.

E. Shift in the BAO Peak Position

Here we quantify the shift in the BAO peak position from the galaxy power spectrum measurements in the presence of the relative velocity effect. Due to the nonlinear effects, the BAO peak is broadened and shifted at the sub-percent level [37, 39]. However, these scale-dependent growth and anomalous nonlinear power can be modeled and marginalized over in measuring the BAO peak position. Following Seo et al. [37], we adopt the template power spectrum to account for the scale-dependent growth and the broad-band power

$$P_t(k) = \left(\sum_{i=0}^2 c_i k^i \right) P_{\text{evo}} \left(\frac{k}{\alpha} \right) + \sum_{i=0}^7 a_i k^i , \quad (30)$$

where three coefficients c_i and eight coefficients a_i are taken as free parameters. Accounting for the damping of the BAO peaks in the linear matter power spectrum, the evolved matter power spectrum is computed as

$$P_{\text{evo}}(k) = [P_{\text{lin}}(k) - P_{\text{nw}}(k)] \exp \left(-\frac{k^2 \Sigma_m^2}{2} \right) + P_{\text{nw}}(k) , \quad (31)$$

where $P_{\text{nw}}(k)$ is the fit to the broad-band power of the linear matter power spectrum [31] and $\Sigma_m = 6.6 h^{-1} \text{Mpc}$ is the degradation parameter of the BAO wiggles at $z = 0.57$ [37]. The template power spectrum $P_t(k)$ is fitted to the galaxy power spectrum with the relative velocity effect, and any deviation of α from unity indicates the shift in the BAO peak position.

Figure 3 shows the shift parameters α in the BAO peak position of the galaxy power spectrum (left) as a function of galaxy bias parameters and its cross-power spectrum (right) with another galaxy sample without the relative velocity effect. The best-fit shift parameter α is obtained by fitting the template power spectrum in Eq. (30) to the galaxy power spectrum in Eq. (9) or the cross-power spectrum in Eq. (12) over

a range $0.02 h \text{Mpc}^{-1} < k < 0.35 h \text{Mpc}^{-1}$. In the absence of the relative velocity effect, the shift in the BAO peak position is at the sub-percent level for various values of the nonlinear galaxy bias parameter b_2 .

For various values of the nonlinear galaxy bias parameters, the shift in the BAO peak position due to the relative velocity effect is less than a percent at $b_r/b_1 \leq 0.01$ for both the auto-power and the cross-power spectra. At a fixed value of the relative velocity bias parameter, the overall level of the BAO peak shift is smaller in the cross-power spectrum (right) than in the auto-power spectrum (left), simply because the galaxy bias parameters for the sample B are smaller than for the sample A and there is no relative velocity effect in the second tracer. Furthermore, the general trend of the BAO peak shift as a function of the relative velocity bias parameter is similar for both cases, since the dominant contribution to the BAO peak shift over the fitting range arises from the coupling of the nonlinear matter evolution and the relative velocity effect shown as long dashed curves in Fig. 2 and their sign remains unchanged in the cross-power spectrum, shifting the BAO peak position to the same direction as in the auto-power spectrum.

For large values of the relative velocity bias parameter, a substantial shift in the BAO peak position may occur, but the auto-power spectrum is better suited for measuring the peak shift due to the relative velocity effect than the cross-power spectrum, when the other galaxy sample is expected to have no relative velocity effect. However, with two galaxy samples, we can construct the sample-variance cancelling combination in Eq. (15) and measure its power spectrum in Fig. 2c to visually identify the relative velocity effect. The fitting procedure of Seo et al. [37] is designed to remove the broad-band shape and isolate the BAO wiggles in the usual galaxy power spectrum, and hence it cannot be used to quantify the shift in the BAO peak position of the power spectrum of the sample-variance cancelling combination in Fig. 2c or its cross-power spectrum in Fig. 2d.

Figure 4 further illustrates the oscillation structure of various relative velocity contributions to the galaxy power spectrum. Compared to the linear matter power spectrum (dotted) in Fig. 4a, gray curves show the one-loop SPT power spectrum (dashed) and the HALOFIT nonlinear matter power spectrum (solid). Though they appear to have quite different oscillation structure, these nonlinear matter power spectra generally yield negligible shift in the BAO peak position as in Fig. 3, when they are fitted with the evolved matter power spectrum $P_{\text{evo}}(k)$ (solid), after marginalizing over the nonlinear scale-dependent growth and the anomalous power with free parameters in Eq. (30).

Figures 4b–4d compare the relative velocity contributions that are fitted with $P_{\text{evo}}(k)$ in Fig. 4a. To remove the broad-band power of the relative velocity contributions and isolate their oscillation structure, we apply various powers of wavenumber k normalized at $0.1 h \text{Mpc}^{-1}$ and divide the contributions to the no-wiggle power spectrum $P_{\text{nw}}(k)$ at $k = 0.1 h \text{Mpc}^{-1}$. A unity at $k = 0.1 h \text{Mpc}^{-1}$ would therefore indicate that its contribution is as large as the no-wiggle power spectrum, if the corresponding bias parameters are set unity. The oscillation structure in the auto-contribution

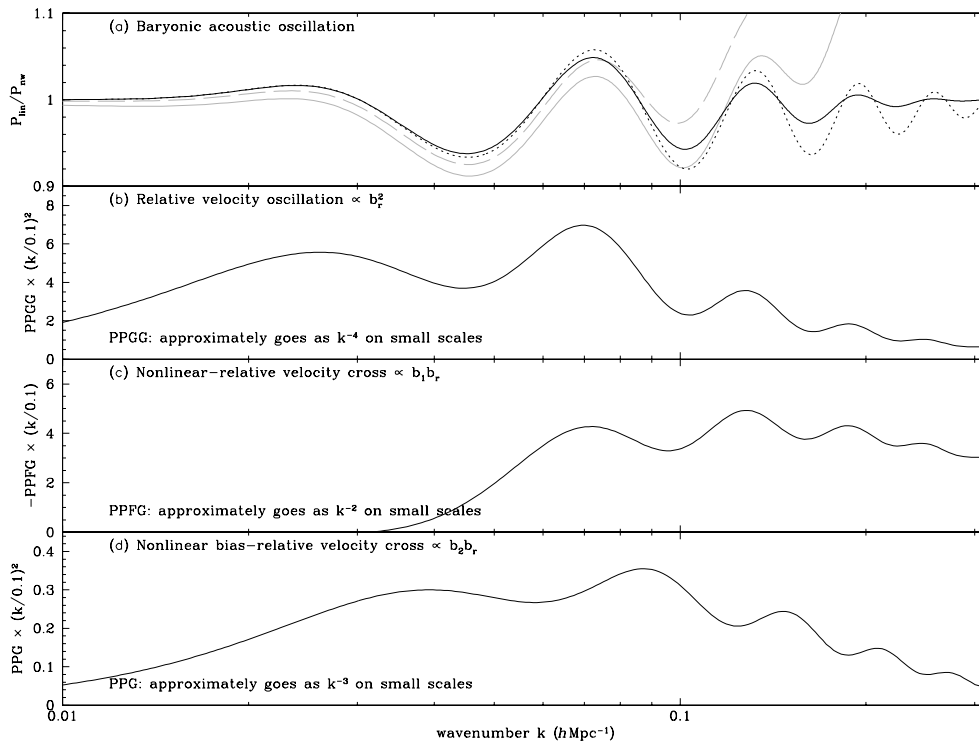


FIG. 4: Baryonic acoustic oscillation and relative velocity contributions at $z = 0$. (a) Ratios to the no-wiggle power spectrum. The BAO template in Eq. (31) is shown as solid curve. Various curves represent the linear matter power spectrum (dotted), one-loop SPT power spectrum (gray dashed), and the HALOFIT nonlinear matter power spectrum (gray solid). (b), (c), (d) Various contributions of the relative velocity effect to the galaxy power spectrum. The amplitude of each component is normalized by the no-wiggle power spectrum at $k = 0.1 \text{ hMpc}^{-1}$ and scaled by various powers of wavenumber to best contrast their oscillation structure. All the bias parameters are set unity for comparison. The contributions PPGG in panel (b) and PPGG in panel (c) are largely in phase with the BAO, while the contribution PPG is out-of-phase.

of the relative velocity effect in Fig. 4b is largely in phase with $P_{\text{evo}}(k)$, but with k^{-4} scaling and b_r^2 , its contribution is rather limited to large scales $k < 0.1 \text{ hMpc}^{-1}$.

Figure 4c describes the cross contribution of the nonlinear matter evolution and the relative velocity effect. With the weak scaling relation k^{-2} and the amplitude at the percent level at $k = 0.1 \text{ hMpc}^{-1}$ for $b_1 \sim 1$ and $b_r \sim 0.01$, the cross contribution affects the shift in the BAO peak position most significantly among various relative velocity contributions over a range $k > 0.1 \text{ hMpc}^{-1}$. The other cross-contribution of the nonlinear galaxy bias and the relative velocity effect is shown in Fig. 4d. With the steep scaling k^{-3} and rather small amplitude, its impact on the BAO peak shift is rather weak, and the nonlinear galaxy bias parameter b_2 often vanishes in certain galaxy samples.

Compared to our previous calculation of the BAO peak shift in the galaxy power spectrum in Yoo et al. [18],² we find that

the overall trend of the BAO peak shift is similar. However, since we use the HALOFIT [32] that better fits the nonlinear matter power spectrum in simulations than the one-loop SPT power spectrum, the overall χ^2 -value of the fit has dramatically improved over the previous calculations. As is evident in Fig. 4a, the one-loop SPT power spectrum significantly deviates from simulations at $k > 0.2 \text{ hMpc}^{-1}$. Though the evolved matter power spectrum $P_{\text{evo}}(k)$ has little oscillation at $k > 0.2 \text{ hMpc}^{-1}$ shown in Fig. 4a, we believe that over the fitting range $k = 0.02 - 0.35 \text{ hMpc}^{-1}$, a more realistic model of the nonlinear matter power spectrum would be better suited in quantifying the shift in the BAO peak position.

F. Template Power Spectrum for Relative Velocity Effect

In the presence of the relative velocity effect, the BAO peak position in the galaxy power spectrum can be shifted as large

² The nonlinear matter power spectrum $P_{\text{NL}}(k)$ in Eq. (4.2) of Yoo et al. [18] is computed by using the one-loop standard perturbation theory (SPT) $P_{\text{NL}}(k) = P_m(k) + P_{13}(k) + P_{22}(k)$. However, there was a factor 2 error in computing the one-loop correction $P_{22}(k)$. With proper calculations of $P_{\text{NL}}(k)$, we find that the shift in the BAO peak position shows

the similar trend as in Fig. 3 — the change of direction in the peak shift for $b_2 < 0$ cases in Fig. 5 of Yoo et al. [18] disappeared. No further significant change arises due to this correction, and Fig. 4 and 6 of Yoo et al. [18] are largely unaffected.

as a few percents shown in Fig. 3, depending on the relative velocity bias parameter. Since the shift in the BAO peak position is *not* due to the nonlinear scale-dependent growth around the BAO peak as shown in Figs. 2 and 4, the evolved linear matter power spectrum $P_{\text{evo}}(k)$ in Eq. (31) is *inadequate* in describing the galaxy power spectrum with the relative velocity effect — the deviation of α from unity in Fig. 3 is the evidence of missing physics, *the relative velocity effect*, not the indication of incorrect cosmological parameters in the fiducial model.

In order to properly account for the relative velocity effect in the galaxy power spectrum and the correlation function, we construct a different template power spectrum that can be used to isolate the shift α in the BAO peak position, only due to the change in cosmology, not due to the relative velocity effect. First, we construct a smooth power spectrum $P_s(k)$ that best describes the broad-band power of the galaxy power spectrum with the relative velocity effect, but without the oscillation structure, in analogy to the no-wiggle power spectrum $P_{\text{nw}}(k)$. Given the galaxy bias parameters $\mathbf{b} = (b_1, b_2, b_r)$, we fit the template power spectrum in Eq. (30) to the galaxy power spectrum $P_g(k|\mathbf{b})$ in Eq. (9) to obtain the peak shift α and the nuisance parameters c_i and a_i in Eq. (30). Second, we construct the smooth power spectrum as

$$P_s(k|\mathbf{b}) = \left(\sum_{i=0}^2 c_i k^i \right) P_{\text{nw}}\left(\frac{k}{\alpha}\right) + \sum_{i=0}^7 a_i k^i, \quad (32)$$

where the fitted parameters (α, c_i, a_i) depend on the galaxy power spectrum $P_g(k|\mathbf{b})$. The evolved matter power spectrum for the relative velocity effect is then defined as

$$P_{\text{evo}}(k|\mathbf{b}) = \left[P_g(k|\mathbf{b}) - P_s(k|\mathbf{b}) \right] \exp\left(-\frac{k^2 \Sigma_m^2}{2}\right) + P_s(k|\mathbf{b}). \quad (33)$$

We repeat the exercise of fitting the template power spectrum $P_t(k)$ in Eq. (30) to the galaxy power spectrum with the relative velocity effect as in Fig. 3, but in this case, with new evolved power spectrum $P_{\text{evo}}(k|\mathbf{b})$ in Eq. (33) for each set of galaxy bias and the relative velocity bias parameters. We find *no* meaningful shift ($\leq 0.05\%$) in all cases, validating the use of the template power spectrum for the relative velocity effect. Further refinement of the evolved power spectrum $P_{\text{evo}}(k|\mathbf{b})$ can be made by iteratively computing the smooth power spectrum $P_s(k|\mathbf{b})$, until no shift is achieved. However, we find that the nuisance parameters of the template power spectrum in Eq. (30) provide a good description of the broad-band power of the galaxy power spectrum with the relative velocity effect and no iteration in most cases is necessary; the maximum shift at one iteration is 0.4% at $b_r/b_1 = 0.1$.

G. Correlation Function

In addition to the galaxy power spectrum measurements, there exist other ways to measure the BAO peak position and hence the distance to the galaxy sample; The galaxy correlation function measurements have been used to identify the

BAO peak position, and the first detection of the BAO scale in galaxy clustering was made [40] by using the correlation function measurements. Here we present the relative velocity effect on the correlation function measurements.

Following Xu et al. [41], we compute the template correlation function, accounting for the nonlinear growth around the BAO peak and the broadening of the BAO feature in the correlation function,

$$\xi_t(r) = B_\xi^2 \xi_{\text{evo}}(\alpha r) + A_\xi(r), \quad (34)$$

where the constant B_ξ effectively marginalizes over the correlation function amplitude, the scale-dependent nonlinear growth around the BAO peak is fitted with

$$A_\xi(r) = \frac{\tilde{a}_1}{r^2} + \frac{\tilde{a}_2}{r} + \tilde{a}_3, \quad (35)$$

and the evolved correlation function is the Fourier transform of the evolved matter power spectrum

$$\xi_{\text{evo}}(r) = \int \frac{dk k^2}{2\pi^2} P_{\text{evo}}(k) j_0(kr) e^{-k^2 \sigma_\xi^2}. \quad (36)$$

We adopted the specific functional form in Eq. (35) to model the scale-dependent growth around the BAO peak, as in Xu et al. [41]. The cut-off scale in the correlation function is set $\sigma_\xi = 1h^{-1}\text{Mpc}$ to ensure that the evolved correlation function over the fitting range $28 < r < 200 h^{-1}\text{Mpc}$ [28] is unaffected by inadequate modeling of the power spectrum at $k \gg \sigma_\xi$.

For predicting the relative velocity effect in the correlation function, we compute Eq. (36) but with $P_{\text{evo}}(k)$ replaced by $P_{\text{evo}}(k|\mathbf{b})$ for the relative velocity effect. However, the best-fit smooth power spectrum $P_s(k|\mathbf{b})$ in Eq. (32) is obtained over a finite fitting range $k = 0.02 - 0.35 h\text{Mpc}^{-1}$, such that when extrapolated beyond the fitting range, it fails to provide a good description of the broad-band shape of the galaxy power spectrum with the relative velocity effect. Therefore, we use the galaxy power spectrum itself for the smooth power spectrum outside the fitting range, noting that the oscillation structure is weak at $k \leq 0.02 h\text{Mpc}^{-1}$ or substantially damped at $k \geq 0.35 h\text{Mpc}^{-1}$.

Figure 5 shows the correlation function (left) of the galaxy sample A and its cross-correlation function (right) with the galaxy sample B . The dotted curves indicates the evolved correlation function in Eq. (36), but its amplitude is multiplied by the galaxy bias parameters $(b_1^A)^2$ and $b_1^A b_1^B$, respectively. As shown in Eq. (34), the evolved correlation function $\xi_{\text{evo}}(r)$ is fitted to the correlation function with nuisance parameters B_ξ and \tilde{a}_i to identify the peak shift α in the correlation function. The correlation functions are scaled to match the dotted curves at $r = 50 h^{-1}\text{Mpc}$, effectively setting the nuisance parameter $B_\xi \approx 1$. Compared to the evolved correlation function, the peak position in the auto-correlation function is shifted to a smaller scale $\alpha > 1$, but its peak is further broadened. These effect are less prominent in the cross-correlation function. As is shown in Fig. 3, the BAO peak shift is $\alpha \sim 1\%$ for the auto-power spectrum and $\alpha \sim 0.2\%$ for the cross-power spectrum

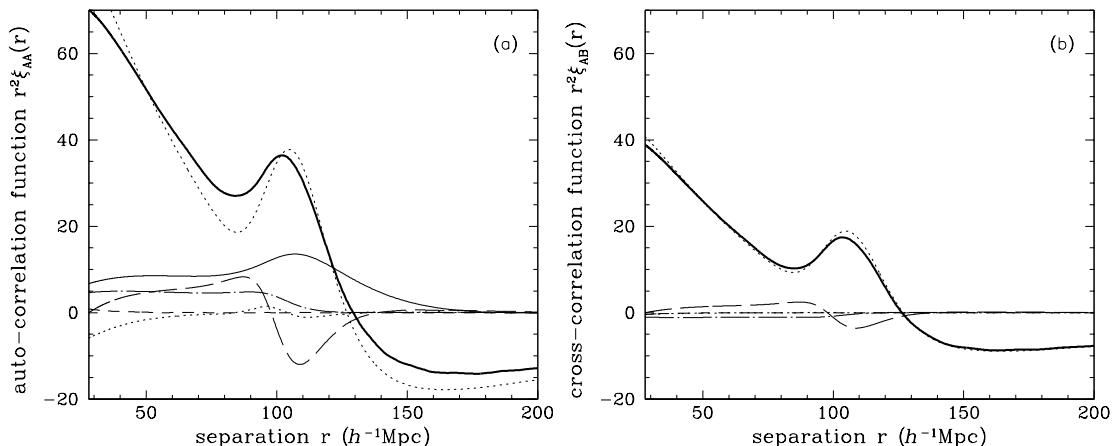


FIG. 5: Auto and cross correlation functions of two galaxy samples. The galaxy sample A is assumed to have bias parameters $(b_1^A, b_2^A) = (2, 1)$ with the relative velocity effect $b_r^A = 0.04$, and the galaxy sample B has $(b_1^B, b_2^B) = (1, -0.4)$ without the relative velocity effect $b_r^B = 0$. As a reference, the dotted curves show the template correlation function in Eq. (36) multiplied by $(b_1^A)^2$ and $b_1^A b_1^B$ in each panel, respectively. The best-fit smooth power spectrum in Eq. (32) is used to damp the BAO wiggles and compute the full correlation function (solid). The correlation functions are scaled to match the template correlation function (dotted) at $r = 50 h^{-1} \text{Mpc}$. Individual contributions to the total correlation functions are shown with line types identical to those in Fig. 2, but its amplitude is multiplied by a factor 2 for better illustration. The BAO peak shift due to the relative velocity effect is more prominent in the auto-correlation function than in the cross-correlation function.

for the fiducial galaxy bias parameters and the relative velocity bias parameter.

Various curves in Fig. 5 around $\xi = 0$ represent the contributions of the individual components to the correlation function with line types as in Fig. 2, but their amplitudes are multiplied by a factor 2 for illustration. They are computed by Fourier transforming the each components in Eqs. (9) and (12), and the damping of the oscillations in these components as in Eq. (33) is neglected for simplicity. The dominant contribution to the BAO peak shift is the cross-correlation (dashed) of the nonlinear matter evolution and the relative velocity effect, followed by the relative velocity correlation (solid). Since the broad-band power will be removed by the nuisance parameters \tilde{a}_i in $A_\xi(r)$, it is the contrast of these components that contributes to the BAO peak shift.

IV. CONSTRAINT ON THE RELATIVE VELOCITY EFFECT FROM THE BOSS

Here we use the SDSS-III Data Release 9 (DR9; Ahn et al. [42]) galaxy sample, denoted as CMASS sample [43]. It comprises approximately 260,000 galaxies with spectroscopic redshift measurements, and their redshift ranges $0.43 < z < 0.7$ with the effective redshift $z_{\text{eff}} = 0.57$ and the number density $\bar{n}_g = 3 \times 10^{-3} (h^{-1} \text{Mpc})^{-3}$. The Baryonic Oscillation Spectroscopic Survey (BOSS; [29]) is part of SDSS-III [44], mapping the spatial distribution of galaxies. The galaxy power spectrum of the SDSS-III DR9 is measured [28] for identifying the BAO peak position and used for other cosmo-

logical purposes (e.g., [45, 46]) and for systematics [47]. We adopt this power spectrum measurements for our analysis of the relative velocity effect and refer to it as the BOSS power spectrum measurements.

The BOSS power spectrum is measured by using the traditional way to estimate the galaxy power spectrum, known as the FKP method [38]. The power spectrum measurements can be expressed as the convolution of the underlying galaxy power spectrum with the survey window function,

$$\hat{P}_g(\mathbf{k}) = \int \frac{d^3 \mathbf{q}}{(2\pi)^3} P_g(\mathbf{q}) \left| \bar{n}_g^w(\mathbf{k} - \mathbf{q}) \right|^2 + P_{\text{shot}}(k), \quad (37)$$

where $P_{\text{shot}}(k)$ is the shot-noise contribution and the survey window function is the Fourier transform of the weighted mean galaxy number density $\bar{n}_g^w(\mathbf{x}) = w(\mathbf{x}) \bar{n}_g(\mathbf{x})$ and is normalized to unity

$$1 = \int \frac{d^3 \mathbf{k}}{(2\pi)^3} |\bar{n}_g^w(\mathbf{k})|^2 = \int d^3 \mathbf{x} [\bar{n}_g^w(\mathbf{x})]^2. \quad (38)$$

To facilitate the computation [28, 48–51], the survey window function is often angle-averaged and discretized into a window matrix $W[k_i][k_j]$, such that the three-dimensional integration of the convolution in Eq. (37) becomes a simple matrix multiplication

$$\hat{P}_g(k_i) = \sum_{k_j} W[k_i][k_j] P_g(k_j) + P_{\text{shot}}(k_i), \quad (39)$$

where the underlying galaxy power spectrum $P_g(k_j)$ is also

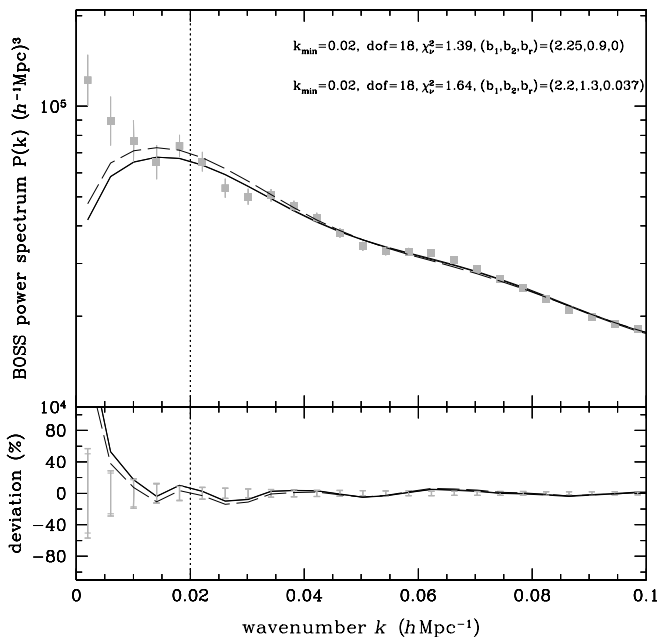


FIG. 6: BOSS power spectrum measurements and the best-fit power spectrum with the relative velocity effect. The galaxy power spectrum $P_g(k|\mathbf{b})$ is fitted to the BOSS measurements (points), accounting for the survey window function and the integral constraints in Eq. (41) over the range $k \leq 0.1 h\text{Mpc}^{-1}$. Two (nearly identical) solid curves show the best-fit galaxy power spectra with the further cut $k_{\min} = 0.02 h\text{Mpc}^{-1}$ and without k_{\min} . The best-fit model is mainly determined over the range $k = 0.02 - 0.1 h\text{Mpc}^{-1}$, but the χ^2 difference is substantial, depending on whether the measurements at $k < 0.02 h\text{Mpc}^{-1}$ are included. The dashed curve shows the model with the largest relative velocity bias parameter that is consistent with the best-fit model at $1-\sigma$ level (see Sec. IV for details).

angle-averaged and the normalization condition becomes

$$1 = \sum_{k_j} W[k_i][k_j]. \quad (40)$$

Furthermore, since the mean galaxy number density \bar{n}_g is unknown and estimated from the survey itself, the measured fluctuation always vanishes at the survey scale, even though the underlying fluctuation may not. This condition, known as the integral constraint, is implemented by shifting the underlying fluctuation to vanish at the survey scale [52]. Therefore, the measured power spectrum involves additional shift due to the integral constraint, and our estimate for the galaxy power spectrum is

$$\hat{P}_g(k_i) = \sum_{k_j} W[k_i][k_j] P_g(k_j) + P_{\text{shot}}(k_i) - \frac{W(k_i)}{W(0)} \sum_{k_j} W[0][k_j] P_g(k_j). \quad (41)$$

Given the galaxy bias parameters $\mathbf{b} = (b_1, b_2, b_r)$, we fit the galaxy power spectrum $P_g(k|\mathbf{b})$ in Eq. (9) to the BOSS power

spectrum measurements, accounting for the survey window function and the integral constraint in Eq. (41). However, for our simple analysis, we keep the cosmological parameters fixed in fitting the BOSS measurements and constraining the relative velocity bias parameter b_r .

Figure 6 illustrates the best-fit galaxy power spectrum (solid) with the relative velocity effect from the BOSS measurements (points). The maximum wavenumber, over which the model is fitted, is set $k_{\max} = 0.1 h\text{Mpc}^{-1}$. Our best-fit model prefers *no* relative velocity effect in the measurements, and the best-fit nonlinear galaxy bias parameters are consistent with the BOSS measurements [45], where they find $(b_1, b_2) = (2.27, 1.02)$. While the best-fit model (solid) provides a good fit to the measurements at $k > 0.02 h\text{Mpc}^{-1}$, there exist substantial deviations at $k < 0.02 h\text{Mpc}^{-1}$, where the measurements are significantly higher. Moreover, the chi-square per degree-of-freedom $\chi^2_\nu = 2.07$ is quite large, demanding further scrutiny.

We repeat the exercise with the minimum wavenumber $k_{\min} = 0.02 h\text{Mpc}^{-1}$ for the fitting range, removing the largest scale measurements, where the measurements are most susceptible to stellar contamination [47]. The goodness of the fit dramatically improves ($\chi^2_\nu = 1.39$), while the best-fit model parameters are almost identical to those obtained without k_{\min} . To further investigate this systematic error, we introduce a nuisance parameter s for the stellar contamination and marginalize over the nuisance parameter, following the procedure in [45]. We find no discernible change in χ^2_ν , compared to that without the nuisance parameter s . However, the best-fit value of s is a few- σ away from $s = 0$, indicating the existence of non-negligible stellar contamination at $k \leq 0.02 h\text{Mpc}^{-1}$. For illustration, the dashed curve shows the model that is consistent with our best-fit model ($\Delta\chi^2 = 2.17^2$) at $1-\sigma$ level but has the largest relative velocity bias parameter. While the relative velocity effect can enhance the power spectrum on large scales $k < 0.02 h\text{Mpc}^{-1}$, it is difficult to explain away the power excess in the largest-scale measurements and maintain the goodness of the fit at $k = 0.02 - 0.1 h\text{Mpc}^{-1}$.

Figure 7 presents the galaxy bias parameter constraints from the BOSS power spectrum measurements. Contours in Fig. 7 depict $\Delta\chi^2 = 1.52^2, 2.49^2, 3.44^2$ regions, covering $1-\sigma, 2-\sigma,$ and $3-\sigma$ ranges in each parameter space from the best-fit value indicated by dots. The constraints are derived with $k_{\min} = 0.02 h\text{Mpc}^{-1}$, while those shown as gray contours are with $k_{\min} = 0$. Again, we find no significant difference in the parameter constraints with different k_{\min} . From the BOSS power spectrum measurements, we derive the constraint on the relative velocity bias parameter $b_r < 0.033$ at the 95% confidence level.

The measurements of the BAO peak position provide model-independent observational constraints on the distance to the galaxy sample (e.g., [28]). However, the possibility of the relative velocity effect in the galaxy sample acts as a systematic error on the BAO measurements, since the BAO peak position can be shifted if the relative velocity effect is present as shown in Fig. 3. Given the probability distribution of the galaxy bias parameters (b_1, b_2) and the relative velocity bias parameter b_r in Fig. 7, we compute the rms shift in the BAO

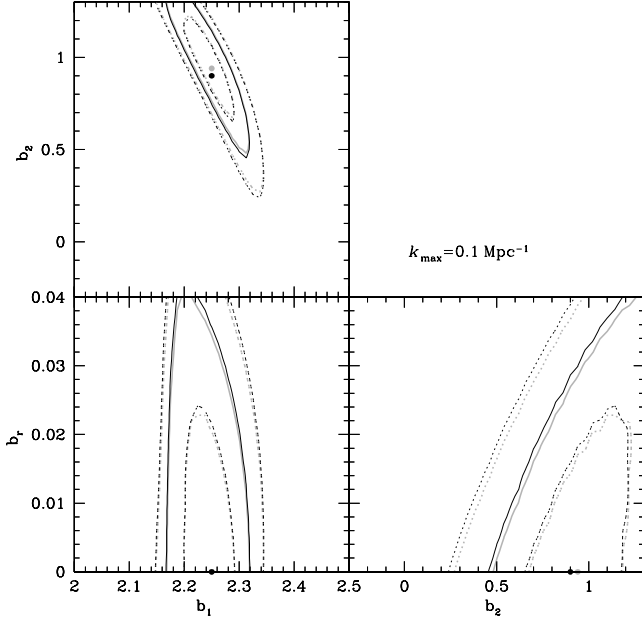


FIG. 7: Constraints on the nonlinear galaxy bias parameters (b_1, b_2) and the relative velocity parameter b_r from the BOSS power spectrum measurements. Contours show 1- σ (dotted), 2- σ (solid), 3- σ (dashed) regions for each two-parameter set. Two nearly overlapping contours represent the constraints with and without $k_{\min} = 0.02 \text{ hMpc}^{-1}$.

peak position

$$\langle \Delta\alpha^2 \rangle = \int db_1 db_2 db_r P(b_1, b_2, b_r) \Delta\alpha^2(b_1, b_2, b_r) = (0.57\%)^2 \quad (42)$$

as our estimate of the systematic error in the BOSS measurements of the BAO peak position, where the shift $\Delta\alpha(b_1, b_2, b_r)$ is shown in Fig. 3 and the probability distribution is assumed to be Gaussian

$$P(b_1, b_2, b_r) \propto \exp[-\Delta\chi^2/2]. \quad (43)$$

Given the current constraint on the BAO peak position is 1.6% ($\alpha = 1.033 \pm 0.017$ [28]), the systematic error due to the relative velocity effect inflates the uncertainty by 5.5% (hence 1.7% in total), assuming that the errors are uncorrelated.

V. FUTURE MEASUREMENTS OF THE RELATIVE VELOCITY EFFECT

In Sec. IV we have derived the constraint on the relative velocity effect from the BOSS measurements. The current constraint is tight, not only because the measurement precision has dramatically improved, but also because the cosmological parameters are held fixed. Looking to the future, we perform a Fisher matrix analysis to forecast how well future galaxy surveys can constrain the relative velocity effects and how much

improvements can be made by adopting the multi-tracer analysis, providing guidance to designing future galaxy surveys.

For definiteness, we consider two galaxy samples, each of which probe volumes $V = 10 (h^{-1}\text{Gpc})^3$ but with different levels of overlapping volume. As our fiducial parameters, we adopt that the galaxy sample A has the bias parameters $\mathbf{b}^A = (b_1, b_2, b_r) = (2, 1, 0.04)$ and $\bar{n}_g^A = 3 \times 10^{-4} (h^{-1}\text{Mpc})^{-3}$, and the galaxy sample B has $\mathbf{b}^B = (b_1, b_2) = (1, -0.4)$ and $\bar{n}_g^B = 10^{-3} (h^{-1}\text{Mpc})^{-3}$. We also consider the cosmological parameter variations parametrized by $\mathbf{c} = (n_s, \alpha_s, \omega_m, \omega_b, \omega_{\text{de}}, w_0, A_s)$, where $h^2 = \omega_m + \omega_{\text{de}}$ is the dimensionless Hubble parameter and we assume a flat universe with a constant dark-energy equation-of-state. Therefore, our fiducial model for two galaxy samples is composed of 12 parameters $\mathbf{p} \equiv (\mathbf{c}, \mathbf{b}^A, \mathbf{b}^B)$, where we explicitly assumed that the relative velocity effect is absent in the galaxy sample B . Last, as an extension of our model, we introduce two additional free parameters for each sample, accounting for the deviation of the shot-noise power spectrum $P_S(k)$ from the usual Poisson noise $P_S(k) = 1/\bar{n}_g$ (e.g., [35, 36, 53]). However, we add a weak prior $\sigma_{P_S} = 1/\bar{n}_g$ on the shot-noise power spectrum to ensure that the shot-noise cannot be completely arbitrary.

To estimate the sensitivity of the power spectrum measurements to the relative velocity effect, we compute the Fisher matrix

$$F_{\mu\nu}(\mathbf{p}) = \sum_{k=k_{\min}}^{k_{\max}} \sum_{i,j} \frac{1}{N_k} f^{ij} \times \frac{\partial P_i(k|\mathbf{p})}{\partial p_\mu} \text{Cov} \left[P_i(k|\mathbf{p}) P_j(k|\mathbf{p}) \right]^{-1} \frac{\partial P_j(k|\mathbf{p})}{\partial p_\nu}, \quad (44)$$

where $k_{\min} = 2\pi/V_s$ and $i, j = AA, BB, AB$, representing the auto- and the cross-power spectra of two galaxy samples A and B . The fractional number of Fourier modes available in the survey is

$$f^{ij} = \begin{cases} 1 & \text{for } i = j = AA, BB \\ V_o/V_s & \text{otherwise} \end{cases}, \quad (45)$$

where V_o is the overlapping volume probed by two galaxy samples. When two samples probe two independent volumes ($V_o = 0$), no cross-power spectrum is used in the Fisher matrix calculation. We also adopt the Planck prior in the cosmological parameter estimation, following the procedure in Albrecht et al. [54]. Therefore, the constraint on the relative velocity bias parameter can be derived as

$$\sigma_{b_r}^2 = [F^{-1}(\mathbf{p})]_{b_r b_r}, \quad (46)$$

after marginalizing over all the cosmological parameters and the remaining bias parameters.

In Fig. 8a the solid (galaxy sample A) and the dashed (galaxy sample B) curves show the constraint on the relative velocity bias parameter from the galaxy power spectrum analysis in a survey of volume $V = 10 (h^{-1}\text{Gpc})^3$. As we increase the maximum wavenumber k_{\max} , the constraints are improved in both cases by lifting the degeneracy among the

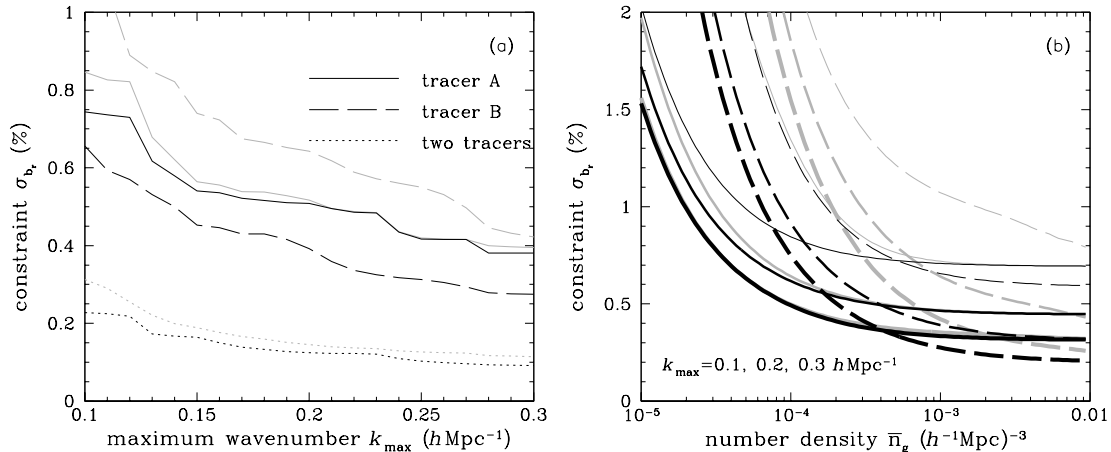


FIG. 8: Constraints on the relative velocity parameters in a survey of volume $V = 10 (h^{-1}\text{Gpc})^3$. The bias parameters of the two galaxy samples are $(b_1, b_2, b_r) = (2, 1, 0.04)$ and $(1, -0.4, 0)$, and their fiducial values of number densities are $n_g = 3 \times 10^{-4}$ and $10^{-3} (h^{-1}\text{Mpc})^{-3}$, respectively. *Left*: Constraint on the relative velocity bias parameter b_r as a function of k_{max} . The cosmological parameters and the remaining bias parameters are marginalized over in deriving the constraint on the relative velocity effect. Dotted curve shows the improvement on the constraint by independently measuring two galaxy samples in the survey (full covariance matrix and their cross-correlation function are taken into account). Gray curves show the constraints, when we allow the shot-noise of each sample to be a free parameter. *Right*: Constraint on b_r as a function of galaxy number density \bar{n}_g . The bias parameters are fixed at their fiducial values. From top to bottom, curves with different thickness represent different k_{max} .

cosmological parameters c and the galaxy bias parameters b . The constraint (dashed) derived from the galaxy sample B is stronger than the constraint (solid) from the galaxy sample A , in large because the shot-noise contribution is lower for the second galaxy sample (with larger number density), but also because the overall power spectrum amplitude is lower $b_1^B < b_1^A$. Another 30% improvements in the constraint arise, if the galaxy bias parameter b_1 and the matter fluctuation normalization A_s are known [18].

The gray curves show the degradation of the constraints, once we allow the shot-noise power spectrum to be free. The degradation is minor for the galaxy sample A , as the relative velocity effect is already present in the galaxy sample A and its contributions to the galaxy power spectrum scale quite differently with a constant shot-noise. However, the dashed curve shows that there exists a strong degradation for the galaxy sample B . Since the relative velocity effect is absent in the galaxy sample B and the nonlinear galaxy bias parameter is negative, the relative velocity contribution can be degenerate with the shot-noise power spectrum with unknown amplitude on broad range of scales.

The dotted curve shows the improved constraints, if two galaxy samples are available in the same survey area, where not only the auto-power spectrum of each sample, but also the cross-power spectra in Fig. 2 can be utilized to constrain the relative velocity bias parameter. A factor of few improvements on the constraint arise, demonstrating that the multi-tracer analysis in Sec. III C extracts more information than the sum of two independent analysis. A sub-percent level con-

straint on the relative velocity bias parameter can be readily achievable, providing a tight constraint on the star formation history in the early Universe. With two tracers combined, the constraint is less sensitive to the uncertainties in the shot-noise power spectra, especially when the maximum wavenumber is large enough that the degeneracy among galaxy bias parameters can be lifted.

The right panel illustrates the dependence of the galaxy number density. We keep the galaxy bias parameters fixed for two galaxy samples, and three curves with different thickness represents different maximum wavenumber k_{max} . At low galaxy number density $\bar{n}_g \rightarrow 0$, the galaxy sample B (dashed) is more shot-noise limited than the galaxy sample A , as the overall amplitude b_1^B is lower. In the opposite limit $\bar{n}_g \rightarrow \infty$, where the measurements are sample-variance limited, they both provide equally strong constraint on the relative velocity bias parameter, when the constraint σ_{b_r} is scaled with b_1 . The constraint σ_{b_r}/b_1 from the galaxy sample A is slightly better in this limit, because the galaxy sample A is assumed to have the relative velocity effect and the galaxy sample B is assumed to be devoid of it, while the difference is rather small, as the relative velocity power spectrum ($\sim b_r^2$) is significant only on large scales. With unknown amplitude of the shot-noise power spectrum, the constraints on the relative velocity bias parameter degrade in all cases at various levels. As the number density increases, most of the information is recovered for the galaxy sample A , but some degeneracy remains unbroken for the galaxy sample B .

Figure 9 further investigates the improvement of the rela-

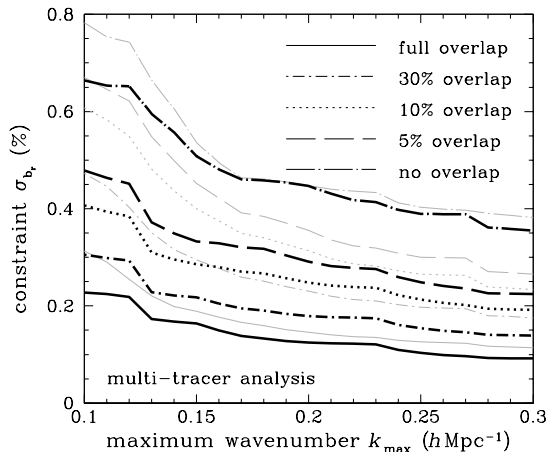


FIG. 9: Multi-tracer analysis of the relative velocity effect. The bias parameters of the two galaxy samples are assumed to have the fiducial values as in Fig. 8. The galaxy sample B is assumed to be independent of the relative velocity effect. The survey volume is $V_s = 10 (h^{-1}\text{Gpc})^3$. The cross-power spectra and the sample-variance cancelling combination are only available when the survey volumes overlap, shown as various curves. For non-overlapping case, the galaxy samples A and B probe two independent survey volumes, and the constraint on the relative velocity effect is derived from the galaxy sample A alone, while the galaxy sample B helps constrain the underlying matter distribution. Gray curves represent the constraints with the same conditions as in black curves, but we additionally marginalize over the unknown amplitudes of the shot-noise power spectra.

tive velocity constraint by using two independent galaxy samples, but with varying degree of overlap in survey volumes. Here we explicitly assume that the galaxy sample B is devoid of the relative velocity effect and the constraint on the relative velocity effect is derived solely by the galaxy sample A . The dot-dashed curve shows the constraints when there is no overlapping volume for two galaxy samples. In this case, the galaxy sample B helps constrain the relative velocity effect by providing constraints on the underlying cosmological parameters and lifting degeneracy in the constraints derived by the galaxy sample A (hence the dot-dashed curve should not be compared to the sum of the solid and the dashed curves in Fig. 8a). As the overlapping volume increases from top to bottom, the constraints on the relative velocity effect improve, but the most dramatic improvement arises when the survey volumes start to overlap (dashed curve). Once two galaxy samples are available for their cross-power spectra in an overlapping volume, they can be used to construct the sample-variance cancelling combination to isolate the relative velocity effect, dramatically improving the leverage to constrain the relative velocity effect.

Gray curves show the degradation due to the uncertainties in the shot-noise power spectra. The constraints inflate by approximately 50% with $k_{\text{max}} = 0.1 h\text{Mpc}^{-1}$, while the

degradation becomes minor at $k_{\text{max}} = 0.3 h\text{Mpc}^{-1}$, consistent with the result in Fig. 8a. The limitation of the multi-tracer analysis in achieving an “infinite” signal-to-noise ratio is the existence of shot-noise. Recently, a new technique has been developed [35, 36] to suppress the shot-noise contribution by applying mass-dependent weights to the galaxy sample. This technique effectively enhances the galaxy number density and the galaxy bias parameters. For simplicity, we repeat the multi-tracer analysis with the galaxy number density $n_g^A = 10^{-3} (h^{-1}\text{Mpc})^{-3}$, approximately three times larger than our fiducial value and the galaxy bias parameters increased by a factor 1.5, as expected from the shot-noise cancelling technique [36], but we kept the properties of the galaxy sample B unchanged. With the shot-noise cancelling technique, the constraint $\sigma_{b_r^A}/b_1^A$ on the relative velocity bias parameter improves, but the improvement is rather weak, since the number density of the galaxy sample A is already large and no substantial gain is achieved by increasing its number density as in Fig. 8b.

VI. DISCUSSION

The supersonic relative velocity effect between baryons and dark matter plays an important role in the formation of the first stars and the earliest baryonic structure by suppressing the dark matter halo abundance, reducing the gas contents in halos, and boosting the minimum halo mass in which gas can cool and form stars [5–9]. Furthermore, these effects could imprint distinct signatures in the 21cm fluctuation signals and affect the reionization history of the Universe [5]. In particular, the enhancement of the 21cm signals at $z \sim 20$ due to the relative velocity effect may be observed in the existing low-frequency radio arrays [15, 16]. Despite the large uncertainties inherent in the nonlinear galaxy formation at low redshifts, it is speculated [5, 12, 18, 19] that this modulation of the relative velocity effect on the early baryonic structure might be inherited by some fraction of stars composing low-redshift massive galaxies or by local patches of intergalactic medium, in which massive galaxies form at later times. Parametrizing our ignorance of the relic amplitude of the remaining relative velocity effect in galaxy samples at low redshifts, we have studied the impact of the relative velocity between baryons and dark matter on the large-scale clustering properties of galaxies.

Drawing on the calculation [18], we have extended the computation of the galaxy power spectrum to the multiple galaxy samples and investigated the synergy effect of the multi-tracer analysis on isolating the relative velocity effect in the galaxy samples. With the small amplitude ($\lesssim 1\%$), if any, of the relative velocity effect that may persist until today, it is somewhat difficult to measure the relative velocity effect in the galaxy power spectrum measurements alone in a model-independent way. However, the situation changes dramatically, once we have another galaxy sample to cross-correlate with, especially when the second galaxy sample is known to have vanishing relative velocity effect, such as in low-mass star forming galaxies that mainly consist of newly

born stars at low redshifts.

Since the acoustic structure of the relative velocity effect in the galaxy power spectrum is similar but out-of-phase with the acoustic structure of the matter and the baryon distributions, the relative velocity effect can shift the BAO peak position by a few percent at a plausible range of the relative velocity bias parameter $b_r = 0 \sim 0.02$, if the relative velocity effect is unaccounted for in determining the BAO peak position. With two distinct galaxy samples measured in an overlapping volume of the survey, their cross-power spectrum and the cross-correlation function can be used to provide an important consistency check to the constraints on the relative velocity effect. On scales $k = 0.02 \sim 0.2 \text{ hMpc}^{-1}$, where the BAO peak position is best measured, the cross-correlation of the relative velocity effect and the nonlinear matter evolution is the dominant contribution to the galaxy power spectrum, shifting the BAO peak position to the same direction in the galaxy auto- and cross-power spectra, although the shift is often reduced in the cross-power spectrum, when the second galaxy sample has negative nonlinear galaxy bias parameter b_2 .

More importantly, the multi-tracer analysis [20] takes advantage of the fact that two galaxy samples trace the same underlying matter distribution, and it allows one to construct a particular combination of two galaxy samples, in which the leading contribution of the matter fluctuation is eliminated, such that the relative velocity effect is the dominant feature in the power spectrum on large scales $k < 0.1 \text{ hMpc}^{-1}$, providing a model-independent way to verify the presence of the relative velocity effect in the galaxy sample. While the leading stochasticity may be eliminated in this sample-variance cancelling combination, the shot-noise contribution still remains in the power spectrum measurements. In order to maximize the utility of the multi-tracer analysis, it is preferred that the second galaxy sample is abundant in number density and has large difference $\Delta b_g = b_1^A - b_1^B$ in their bias factors (see also [21]), which enhances the contrast of the relative velocity effect to the shot-noise contribution in the galaxy power spectrum.

Using the publicly available BOSS power spectrum measurements [28] of the CMASS galaxy sample [43] from the SDSS-III Data Release 9 [42], we have derived the constraint on the relative velocity effect — the relative velocity bias parameter is constrained $b_r < 0.033$ at the 95% confidence level from the BOSS power spectrum at $k = 0.02 - 0.1 \text{ hMpc}^{-1}$. Though the constraint may be further improved by extending the fitting range, the goodness-of-the-fit substantially degrades, as the systematic error in the theoretical modeling becomes non-negligible. Hence we take the conservative estimate of the upper limit on the relative velocity effect as $b_r < 0.033$. The constraint on the relative velocity bias parameter yields the systematic error $\langle \Delta \alpha^2 \rangle^{1/2} = 0.57\%$ on the BOSS measurements of the BAO peak position at $z = 0.57$. Compared to the current observational error $\Delta \alpha = 1.7\%$, the systematic error due to the relative velocity effect is negligible.

Consider a population of the first stars that form at very early time, in which the relative velocity effect is the dominant mechanism, modulating the spatial fluctuation of the stel-

lar population: $n_* \simeq \bar{n}_*(1 + u_r^2)$. The relative velocity bias parameter is of order unity at early times [5], and $\delta_m \ll 1$. In contrast, typical galaxy samples including the CMASS sample are composed of ordinary stars without the relative velocity effect, and those galaxy samples are well described by the linear bias relation on large scales today: $n_\odot \simeq \bar{n}_\odot(1 + b \delta_m)$.³ Assuming that the CMASS galaxy sample is composed of these two populations of stars, we can relate the relic amplitude b_r of the relative velocity effect to the fraction of the first stars in the CMASS galaxy sample as

$$n_g^{\text{CMASS}} = \bar{n}_\odot(1 + b \delta_m) + \bar{n}_*(1 + u_r^2) \simeq \bar{n}_g(1 + b \delta_m + f_* u_r^2), \quad (47)$$

where we assumed $\bar{n}_g \simeq \bar{n}_\odot \gg \bar{n}_*$ and $f_* = \bar{n}_*/\bar{n}_g \ll 1$. The dimensionless relative velocity u_r is normalized and largely independent of time. The constraint on the relative velocity bias parameter is, therefore, directly linked with the fraction of the first stars in the CMASS galaxy sample, and we derive the upper limit on the fraction of the first stars as 3.3% in the CMASS galaxy sample at the 95% confidence level.

We used “first stars” to refer to a stellar population, of which the spatial distribution is modulated by the relative velocity effect at early times, as opposed to the “ordinary stars” without the relative velocity effect at late times. Our constraint applies to the fraction of those stars with the relative velocity effect, not to the fraction of “the first stars” that are known as the population III stars, as their lifetime is very short [55]. In this regard, our toy model is a phenomenological description, agnostic of the merger history and the stellar evolution. A more thorough modeling of the formation history would be interesting, especially when the relative velocity effect is detected, but it is beyond the scope of the current investigation.

Furthermore, regarding the interpretation of our upper limit, a few more caveats are in order. First, we held the cosmological parameters fixed as the best-fit parameter set derived in the *Planck* result [1]. With the tight constraints on the cosmological parameters, variations of the BAO peak position are negligible among permitted sets of cosmological parameters. We suspect that a full analysis of the galaxy power spectrum with cosmological parameter variation is unlikely to change the upper limit. However, we note that a cosmological parameter set substantially different from our fiducial model could favor the presence of the relative velocity effect, albeit marginal ($\sigma_{b_r} \sim 3\%$), since the BAO scale would be somewhat different in the assumed cosmology. Second, the redshift-space distortion is neglected in the power spectrum analysis. However, on large scales, the redshift-space distortion only enhances the power by a factor $1 + 2\beta/3 + \beta^2/5$ in a scale-independent manner, where β is the anisotropy parameter. Since the relative velocity effect is measured from its scale-dependent oscillations, modeling of the redshift-space distortion will leave the derived constraint unchanged, but we

³ Despite our notation (n_* , n_\odot) for two different populations of stars, they represent the galaxy number densities on large scales that are entirely made of each stellar population. They should not be confused with stellar number densities in some local regions.

suspect that it would reduce our estimate of the galaxy bias factor by 13% with $\beta \simeq 0.39$ to a more reasonable value $b_1 \simeq 2.0$.

Looking to the future, we have forecasted the constraint on the relative velocity effect derivable from the multi-tracer analysis in future galaxy surveys. With two galaxy samples in a survey of $V = 10 (h^{-1}\text{Gpc})^3$, the multi-tracer analysis can achieve a 0.1–0.2% level constraint on the relative velocity bias parameter, improving the constraint by a factor of $3 \sim 5$ compared to the single tracer analysis. Since future galaxy surveys aim to measure galaxies at higher redshift $z \gg 0.5$, the impact of the relative velocity effect on the galaxy power spectrum, if present in the galaxy samples, could be larger, providing an opportunity to detect the relative velocity effect in galaxy surveys and better understand the galaxy formation history before reionization.

Acknowledgments

We thank Florian Beutler and Chris Blake for useful comments and Will Percival for providing the BOSS power spectrum measurements in electronic form. This work is supported by the Swiss National Foundation (SNF) under con-

tract 200021-116696/1 and WCU grant R32-10130. J.Y. is supported by the SNF Ambizione Grant.

Funding for SDSS-III has been provided by the Alfred P. Sloan Foundation, the Participating Institutions, the National Science Foundation, and the U.S. Department of Energy Office of Science. The SDSS-III web site is <http://www.sdss3.org/>.

SDSS-III is managed by the Astrophysical Research Consortium for the Participating Institutions of the SDSS-III Collaboration including the University of Arizona, the Brazilian Participation Group, Brookhaven National Laboratory, University of Cambridge, Carnegie Mellon University, University of Florida, the French Participation Group, the German Participation Group, Harvard University, the Instituto de Astrofísica de Canarias, the Michigan State/Notre Dame/JINA Participation Group, Johns Hopkins University, Lawrence Berkeley National Laboratory, Max Planck Institute for Astrophysics, Max Planck Institute for Extraterrestrial Physics, New Mexico State University, New York University, Ohio State University, Pennsylvania State University, University of Portsmouth, Princeton University, the Spanish Participation Group, University of Tokyo, University of Utah, Vanderbilt University, University of Virginia, University of Washington, and Yale University.

-
- [1] Planck Collaboration, P. A. R. Ade, N. Aghanim, C. Armitage-Caplan, M. Arnaud, M. Ashdown, F. Atrio-Barandela, J. Aumont, C. Baccigalupi, A. J. Banday, et al., ArXiv e-prints (2013), 1303.5076.
 - [2] R. Barkana and A. Loeb, Reports on Progress in Physics **70**, 627 (2007), arXiv:0611541.
 - [3] S. R. Furlanetto, S. P. Oh, and F. H. Briggs, Phys. Rep. **433**, 181 (2006), arXiv:0608032.
 - [4] D. Tselikhovich and C. Hirata, Phys. Rev. D **82**, 083520 (2010), 1005.2416.
 - [5] N. Dalal, U. Pen, and U. Seljak, J. Cosmol. Astropart. Phys. **11**, 7 (2010), 1009.4704.
 - [6] D. Tselikhovich, R. Barkana, and C. M. Hirata, Mon. Not. R. Astron. Soc. **418**, 906 (2011), 1012.2574.
 - [7] A. Fialkov, R. Barkana, D. Tselikhovich, and C. M. Hirata, Mon. Not. R. Astron. Soc. **424**, 1335 (2012), 1110.2111.
 - [8] M. McQuinn and R. M. O’Leary, Astrophys. J. **760**, 3 (2012), 1204.1345.
 - [9] S. Naoz, N. Yoshida, and N. Y. Gnedin, Astrophys. J. **747**, 128 (2012), 1108.5176.
 - [10] U. Maio, L. V. E. Koopmans, and B. Ciardi, Mon. Not. R. Astron. Soc. **412**, L40 (2011), 1011.4006.
 - [11] A. Stacy, V. Bromm, and A. Loeb, Astrophys. J. Lett. **730**, L1 (2011), 1011.4512.
 - [12] T. H. Greif, S. D. M. White, R. S. Klessen, and V. Springel, Astrophys. J. **736**, 147 (2011), 1101.5493.
 - [13] S. Naoz, N. Yoshida, and N. Y. Gnedin, Astrophys. J. **763**, 27 (2013), 1207.5515.
 - [14] R. M. O’Leary and M. McQuinn, Astrophys. J. **760**, 4 (2012), 1204.1344.
 - [15] E. Visbal, R. Barkana, A. Fialkov, D. Tselikhovich, and C. M. Hirata, Nature (London) **487**, 70 (2012), 1201.1005.
 - [16] A. Fialkov, R. Barkana, E. Visbal, D. Tselikhovich, and C. M. Hirata, ArXiv e-prints (2012), 1212.0513.
 - [17] J. M. Bittner and A. Loeb, ArXiv e-prints (2011), 1110.4659.
 - [18] J. Yoo, N. Dalal, and U. Seljak, J. Cosmol. Astropart. Phys. **7**, 018 (2011), 1105.3732.
 - [19] S. Ferraro, K. M. Smith, and C. Dvorkin, Phys. Rev. D **85**, 043523 (2012), 1110.2182.
 - [20] U. Seljak, Phys. Rev. Lett. **102**, 021302 (2009), 0807.1770.
 - [21] P. McDonald and U. Seljak, J. Cosmol. Astropart. Phys. **10**, 7 (2009), 0810.0323.
 - [22] G. M. Bernstein and Y.-C. Cai, Mon. Not. R. Astron. Soc. **416**, 3009 (2011), 1104.3862.
 - [23] Y.-C. Cai, G. Bernstein, and R. K. Sheth, Mon. Not. R. Astron. Soc. **412**, 995 (2011), 1007.3500.
 - [24] N. Hamaus, U. Seljak, and V. Desjacques, Phys. Rev. D **86**, 103513 (2012), 1207.1102.
 - [25] P. McDonald, J. Cosmol. Astropart. Phys. **11**, 26 (2009), 0907.5220.
 - [26] N. Hamaus, U. Seljak, and V. Desjacques, Phys. Rev. D **84**, 083509 (2011), 1104.2321.
 - [27] J. Yoo, N. Hamaus, U. Seljak, and M. Zaldarriaga, Phys. Rev. D **86**, 063514 (2012), 1206.5809.
 - [28] L. Anderson, E. Aubourg, S. Bailey, D. Bizyaev, M. Blanton, A. S. Bolton, J. Brinkmann, J. R. Brownstein, et al., Mon. Not. R. Astron. Soc. **427**, 3435 (2012), 1203.6594.
 - [29] D. Schlegel, M. White, and D. Eisenstein, in *astro2010: The Astronomy and Astrophysics Decadal Survey* (2009), vol. 2010, p. 314, 0902.4680.
 - [30] U. Seljak and M. Zaldarriaga, Astrophys. J. **469**, 437 (1996), astro-ph/9603033.
 - [31] D. J. Eisenstein and W. Hu, Astrophys. J. **496**, 605 (1998), arXiv:astro-ph/9709112.
 - [32] R. E. Smith, J. A. Peacock, A. Jenkins, S. D. M. White, C. S. Frenk, F. R. Pearce, P. A. Thomas, G. Efstathiou, and

- H. M. P. Couchman, *Mon. Not. R. Astron. Soc.* **341**, 1311 (2003), arXiv:astro-ph/0207664.
- [33] D. H. Weinberg, M. J. Mortonson, D. J. Eisenstein, C. Hirata, A. G. Riess, and E. Rozo, *ArXiv e-prints* (2012), arXiv:1201.2434.
- [34] C. Blake, R. J. Jurek, S. Brough, M. Colless, W. Couch, S. Croom, T. Davis, M. J. Drinkwater, D. Forbes, K. Glazebrook, et al., *Mon. Not. R. Astron. Soc.* **395**, 240 (2009), 0901.2587.
- [35] U. Seljak, N. Hamaus, and V. Desjacques, *Phys. Rev. Lett.* **103**, 091303 (2009), 0904.2963.
- [36] N. Hamaus, U. Seljak, V. Desjacques, R. E. Smith, and T. Baldauf, *Phys. Rev. D* **82**, 043515 (2010), 1004.5377.
- [37] H.-J. Seo, E. R. Siegel, D. J. Eisenstein, and M. White, *Astrophys. J.* **686**, 13 (2008), 0805.0117.
- [38] H. A. Feldman, N. Kaiser, and J. A. Peacock, *Astrophys. J.* **426**, 23 (1994), arXiv:astro-ph/9304022.
- [39] B. D. Sherwin and M. Zaldarriaga, *Phys. Rev. D* **85**, 103523 (2012), 1202.3998.
- [40] D. J. Eisenstein, M. Blanton, I. Zehavi, N. Bahcall, J. Brinkmann, J. Loveday, A. Meiksin, and D. Schneider, *Astrophys. J.* **619**, 178 (2005), arXiv:astro-ph/0411559.
- [41] X. Xu, N. Padmanabhan, D. J. Eisenstein, K. T. Mehta, and A. J. Cuesta, *Mon. Not. R. Astron. Soc.* **427**, 2146 (2012), 1202.0091.
- [42] C. P. Ahn, R. Alexandroff, C. Allende Prieto, S. F. Anderson, T. Anderton, B. H. Andrews, É. Aubourg, S. Bailey, E. Balbinot, R. Barnes, et al., *Astrophys. J. Suppl. Ser.* **203**, 21 (2012), 1207.7137.
- [43] M. White, M. Blanton, A. Bolton, D. Schlegel, J. Tinker, A. Berlind, L. da Costa, E. Kazin, Y.-T. Lin, M. Maia, et al., *Astrophys. J.* **728**, 126 (2011), 1010.4915.
- [44] D. J. Eisenstein, D. H. Weinberg, E. Agol, H. Aihara, C. Allende Prieto, S. F. Anderson, J. A. Arns, É. Aubourg, S. Bailey, E. Balbinot, et al., *Astron. J.* **142**, 72 (2011), 1101.1529.
- [45] G.-B. Zhao, S. Saito, W. J. Percival, A. J. Ross, F. Montesano, M. Viel, D. P. Schneider, D. J. Ernst, M. Manera, J. Miralda-Escude, et al. (2012), 1211.3741.
- [46] E. A. Kazin, A. G. Sanchez, A. J. Cuesta, F. Beutler, C.-H. Chuang, D. J. Eisenstein, M. Manera, N. Padmanabhan, W. J. Percival, F. Prada, et al., *ArXiv e-prints* (2013), 1303.4391.
- [47] A. J. Ross, W. J. Percival, A. G. Sánchez, L. Samushia, S. Ho, E. Kazin, M. Manera, et al., *Mon. Not. R. Astron. Soc.* **424**, 564 (2012), 1203.6499.
- [48] S. Cole, W. J. Percival, et al., *Mon. Not. R. Astron. Soc.* **362**, 505 (2005), astro-ph/0501174.
- [49] W. J. Percival, R. C. Nichol, D. J. Eisenstein, D. H. Weinberg, M. Fukugita, A. C. Pope, D. P. Schneider, A. S. Szalay, M. S. Vogeley, I. Zehavi, et al., *Astrophys. J.* **657**, 51 (2007), arXiv:astro-ph/0608635.
- [50] W. J. Percival, B. A. Reid, D. J. Eisenstein, N. A. Bahcall, T. Budavari, J. A. Frieman, et al., *Mon. Not. R. Astron. Soc.* **401**, 2148 (2010), 0907.1660.
- [51] C. Blake, S. Brough, et al., *Mon. Not. R. Astron. Soc.* **406**, 803 (2010), 1003.5721.
- [52] J. A. Peacock and D. Nicholson, *Mon. Not. R. Astron. Soc.* **253**, 307 (1991).
- [53] T. Baldauf, U. Seljak, R. E. Smith, N. Hamaus, and V. Desjacques, *ArXiv e-prints* (2013), 1305.2917.
- [54] A. Albrecht et al., *ArXiv Astrophysics e-prints* (2006), astro-ph/0609591.
- [55] M. Tegmark, J. Silk, M. J. Rees, A. Blanchard, T. Abel, and F. Palla, *Astrophys. J.* **474**, 1 (1997), arXiv:9603007.